iScience

CellPress
OPEN ACCESS

Article

Fine-tuned KDM1A alternative splicing regulates human cardiomyogenesis through an enzymatic-independent mechanism

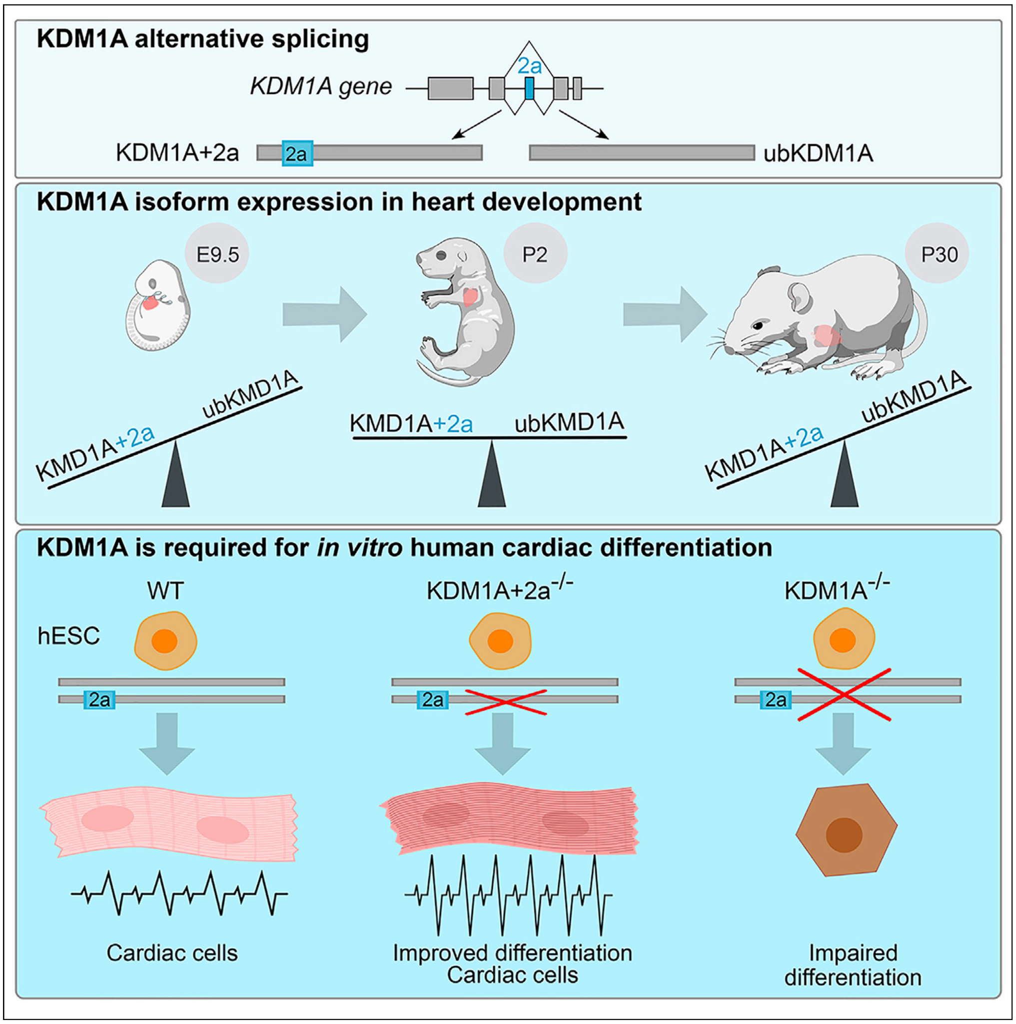

Veronica Astro, Gustavo Ramirez-Calderon, Roberta Pennucci, ..., Elena Battaglioli, Andrea Mattevi, Antonio Adamo

antonio.adamo@kaust.edu.sa

Highlights

ubKDM1A and KDM1A+2a isoforms are fine-tuned during fetal cardiac development

Depletion of KDM1A isoforms impairs hESC differentiation into cardiac cells

KDM1A+2a ablation enhances the expression of key cardiac markers

KDM1A isoforms exhibit enzymatic-independent divergent roles during cardiogenesis

Astro et al., iScience *25*, 104665
July 15, 2022
https://doi.org/10.1016/j.isci.2022.104665

iScience

CellPress OPEN ACCESS

Article

Fine-tuned KDM1A alternative splicing regulates human cardiomyogenesis through an enzymatic-independent mechanism

Veronica Astro,[1] Gustavo Ramirez-Calderon,[1] Roberta Pennucci,[1] Jonatan Caroli,[2] Alfonso Saera-Vila,[3] Kelly Cardona-Londoño,[1] Chiara Forastieri,[4] Elisabetta Fiacco,[1] Fatima Maksoud,[1] Maryam Alowaysi,[1] Elisa Sogne,[1] Andrea Falqui,[1] Federico Gonzàlez,[5] Nuria Montserrat,[5,6,7] Elena Battaglioli,[4] Andrea Mattevi,[2] and Antonio Adamo[1,8,*]

SUMMARY

The histone demethylase KDM1A is a multi-faceted regulator of vital developmental processes, including mesodermal and cardiac tube formation during gastrulation. However, it is unknown whether the fine-tuning of KDM1A splicing isoforms, already shown to regulate neuronal maturation, is crucial for the specification and maintenance of cell identity during cardiogenesis. Here, we discovered a temporal modulation of ubKDM1A and KDM1A+2a during human and mice fetal cardiac development and evaluated their impact on the regulation of cardiac differentiation. We revealed a severely impaired cardiac differentiation in KDM1A$^{-/-}$ hESCs that can be rescued by re-expressing ubKDM1A or catalytically impaired ubKDM1A-K661A, but not by KDM1A+2a or KDM1A+2a-K661A. Conversely, KDM1A+2a$^{-/-}$ hESCs give rise to functional cardiac cells, displaying increased beating amplitude and frequency and enhanced expression of critical cardiogenic markers. Our findings prove the existence of a divergent scaffolding role of KDM1A splice variants, independent of their enzymatic activity, during hESC differentiation into cardiac cells.

INTRODUCTION

Alternative splicing is a key cellular phenomenon allowing the expansion of genome complexity and diversification of protein functions. During cardiac development, alternative splicing regulates the transition from embryonic to fetal and neonatal heart (Cooper and Ordahl, 1985; Giudice et al., 2014; Godt et al., 1993; Kalsotra et al., 2008; McAuliffe et al., 1990; Pervolaraki et al., 2018). Nowadays, it is also becoming clear that altered regulation of splicing causes an increasing number of cardiac diseases (Cooper and Ordahl, 1985; Gi et al., 2020; Meder et al., 2017; Neagoe et al., 2002; Schoenauer et al., 2011; Scotti and Swanson, 2016).

Lysine-specific demethylase LSD1 (also known as KDM1A) is a flavin-dependent demethylase of mono- and di-methylated Lysine4 (K4) and Lysine9 (K9) of histone H3 whose enzymatic function is associated with multiple cellular processes, including embryo development, stem cell maintenance, neuronal specification, hematopoiesis and androgen response (Adamo et al., 2011; Metzger et al., 2005; Niebel et al., 2014; Wang et al., 2008; Whyte et al., 2013; Zibetti et al., 2010). These multifaceted functions are exerted through the recruitment of KDM1A by various transcription factors (TFs) in a tissue-specific manner.

Four alternatively spliced variants of KDM1A, two ubiquitous (hereafter ubKDM1A and KDM1A+2a) and two restricted to the neuronal compartment (hereafter nKDM1A + E8a and nKDM1A+2a+8a) have been described so far (Figure 1A) (Zibetti et al., 2010). The neuronal isoforms are characterized by the inclusion of a twelve base pairs microexon coding for an in-frame stretch of only four amino acids (E8a) at the level of the amino oxidase domain. Seminal studies performed using nKDM1A specific knock-out (KO) mice linked nKDM1A isoforms to stress response, emotional behavior, memory consolidation, and molecular stress sensors (Rusconi et al., 2015, 2016). Moreover, it has been proposed that the E8a inclusion confers KDM1A different substrate specificity mediated by the interaction with alternative cofactors (Laurent

[1] Biological and Environmental Science and Engineering Division, King Abdullah University of Science and Technology, Thuwal 23955-6900, Saudi Arabia

[2] Department of Biology and Biotechnology, University of Pavia, 27100 Pavia, Italy

[3] Sequentia Biotech SL, Barcelona 08005, Spain

[4] Department of Medical Biotechnology and Translational Medicine, University of Milan, Via Fratelli Cervi 93, 20090 Segrate, Milan, Italy

[5] Pluripotency for Organ Regeneration, Institute for Bioengineering of Catalonia (IBEC), The Barcelona Institute of Science and Technology (BIST), Barcelona, Spain

[6] Centro de Investigación Biomédica en Red en Bioingeniería, Biomateriales y Nanomedicina, Barcelona, Spain

[7] Institució Catalana de Recerca i Estudis Avançats (ICREA), Barcelona, Spain

[8] Lead contact

*Correspondence: antonio.adamo@kaust.edu.sa

https://doi.org/10.1016/j.isci.2022.104665

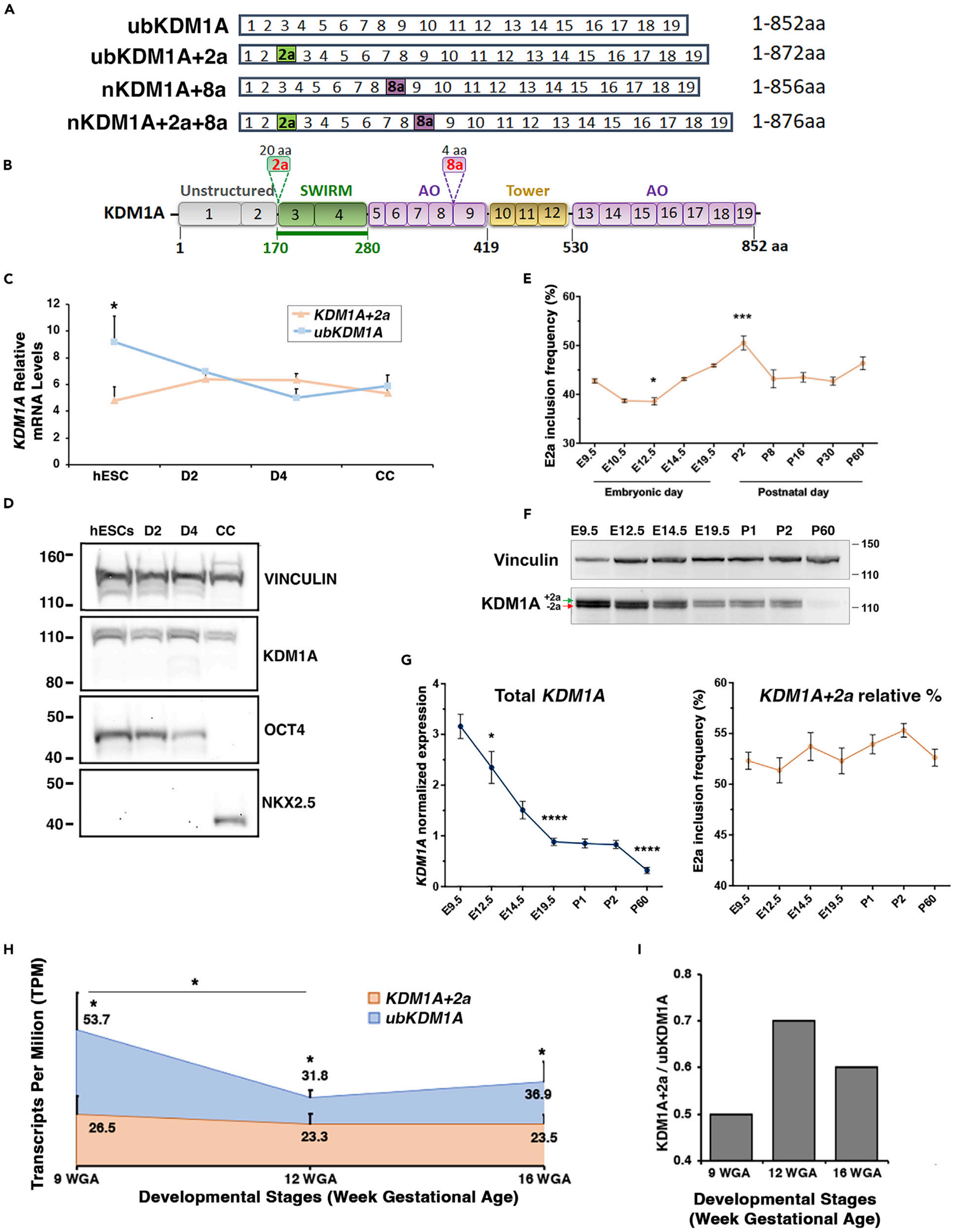
A
ubKDM1A
1 2 3 4 5 6 7 8 9 10 11 12 13 14 15 16 17 18 19
1-852aa
ubKDM1A+2a
1 2 2a 3 4 5 6 7 8 9 10 11 12 13 14 15 16 17 18 19
1-872aa
nKDM1A+8a
1 2 3 4 5 6 7 8 8a 9 10 11 12 13 14 15 16 17 18 19
1-856aa
nKDM1A+2a+8a
1 2 2a 3 4 5 6 7 8 8a 9 10 11 12 13 14 15 16 17 18 19
1-876aa
B
20 aa
2a
4 aa
8a
Unstructured
SWIRM
AO
Tower
AO
KDM1A
1 2 3 4 5 6 7 8 9 10 11 12 13 14 15 16 17 18 19
1
170
280
419
530
852 aa
C
KDM1A Relative mRNA Levels
0 2 4 6 8 10 12
*
KDM1A+2a
ubKDM1A
hESC
D2
D4
CC
D
hESCs D2 D4 CC
160
110
VINCULIN
110
80
KDM1A
50
40
OCT4
50
40
NKX2.5
E
E2a inclusion frequency (%)
30 40 50 60
*
***
E9.5 E10.5 E12.5 E14.5 E19.5 P2 P8 P16 P30 P60
Embryonic day
Postnatal day
F
E9.5 E12.5 E14.5 E19.5 P1 P2 P60
Vinculin
150
110
KDM1A
+2a
-2a
110
G
Total KDM1A
KDM1A normalized expression
0 1 2 3 4
*
****
****
E9.5 E12.5 E14.5 E19.5 P1 P2 P60
KDM1A+2a relative %
E2a inclusion frequency (%)
40 45 50 55 60
E9.5 E12.5 E14.5 E19.5 P1 P2 P60
H
Transcripts Per Milion (TPM)
*
*
53.7
26.5
*
31.8
23.3
*
36.9
23.5
KDM1A+2a
ubKDM1A
9 WGA
12 WGA
16 WGA
Developmental Stages (Week Gestational Age)
I
KDM1A+2a / ubKDM1A
0.4 0.5 0.6 0.7 0.8
9 WGA
12 WGA
16 WGA
Developmental Stages (Week Gestational Age)

Figure 1. KDM1A isoforms are dynamically regulated during cardiomyogenesis

(A) The *KDM1A* gene codes for four variants, differing for the inclusion of two alternatively spliced exons, E2a and E8a. ub = ubiquitous; n = neuronal.
(B) Schematic of KDM1A protein. AO, amino oxidase.
(C) Transcript levels of *KDM1A* isoforms normalized to the internal control *TBP* (TATA-binding protein) detected by variant-specific Taqman probes during cardiac differentiation. CC, contracting cardiac cells.
(D) Western blot showing KDM1A variant protein expression during the differentiation of hESCs into beating cells.
(E) Graph showing the percentage of E2a inclusion in mice fetal hearts collected at the indicated developmental stages, assessed by rqfRT-PCR.
(F) Western blot showing the fluctuation of KDM1A variants in mice heart extracts at the indicated developmental stages.
(G) Graph showing total KDM1A protein levels during mice cardiogenesis (left) and the percentage of E2a protein inclusion in mice hearts collected at the indicated time points (right). One-way ANOVA, Dunnett's post-hoc test (*$p < 0.05$, ***$p < 0.001$, ****$p < 0.0001$ referred to E9.5).
(H) Transcripts per Million (TPM) Reads identified by Kallisto for *KDM1A* variants in human fetal hearts at 9,12 and 16 WGA. Bars are ± STD of three independent RNA samples. *$p > 0.05$ (Student's *t* test).
(I) Graph showing *KDM1A+2a/ubKDM1A* mRNA expression ratio in human fetal hearts.
See also Figure S1.

et al., 2015; Wang et al., 2015). KDM1A+2a includes an in-frame exon (E2a), encoding a stretch of 20 amino acids inserted within the intrinsically disordered N-terminal of KDM1A, in the immediate proximity of the SWIRM domain. The SWIRM domain contains a tract of about 85 evolutionarily conserved amino acids found in chromatin-modulating complexes associated with DNA binding and nucleosome recognition (Tochio et al., 2006). Notably, the SWIRM domain is in spatial contiguity with the enzymatic pocket of KDM1A. This domain forms an hydrophobic cleft that might mediate the interaction of the enzyme with the N-tail of histone H3 (Da et al., 2006; Tochio et al., 2006).

All these data acquire further relevance in light of studies demonstrating a role for KDM1A during development *in vitro* and *in vivo* (Adamo et al., 2011; Fei et al., 2021; Foster et al., 2010; Tamaoki et al., 2020; Whyte et al., 2013). In mice, at the earliest stages of development, the expression of KDM1A is first detected after zygote genome activation at the morula stage (Zhu et al., 2014). As the embryo development proceeds, KDM1A regulates the differentiation into trophoblast and epiblast during blastocyst formation (Macfarlan et al., 2011). KDM1A-KO mice die around E6.5-E7.5 because of major gastrulation defects (Macfarlan et al., 2011). In human embryonic stem cells (hESCs), KDM1A negatively regulates meso-endodermal developmental genes by fine-tuning the histone H3K4 methylation status at the level of poised domains (Adamo et al., 2011; Foster et al., 2010). Intriguingly, E2a inclusion within *KDM1A* transcripts is conserved in mammals and birds among all vertebrates (Zibetti et al., 2010). Mammals and birds have a double circulatory system in which the heart is wholly divided into right and left sides, resulting in the inclusion of deoxygenated and oxygenated blood. The acquisition and conservation of E2a in mammals and birds might represent an evolutionary strategy to develop a more efficient cardiocirculatory system compatible with the energetic request of homeothermic animals (Andrés-Delgado and Mercader, 2016; Epstein, 2010).

To fill the knowledge gap on the role of KDM1A isoforms during cardiac development, we profiled the dynamic changes of its splicing variants in human and mice fetal hearts at different prenatal stages. We performed *in vitro* cardiac differentiation of control and isoform-specific KDM1A KO hESCs and discovered that their depletion leads to severe differentiation defects. We also defined the biochemical and genome-wide binding properties of E2a insertion through *in vitro* binding assays, mass-spectrometry, and chromatin immunoprecipitation (ChIP) analysis, and proved that E2a inclusion serves to finely balance the powerful functions of the ubKDM1A variant. Finally, we demonstrated a demethylase-independent role for KDM1A isoforms during *in vitro* cardiogenesis through genetic rescue experiments with wild-type (WT) isoform-specific or enzymatic-deficient KDM1A-K661A vectors and pharmacological inhibition of KDM1A.

RESULTS

Ubiquitously expressed KDM1A variants are dynamically regulated during cardiac development

Previous studies have shown that KDM1A knock-down in hESCs leads to the aberrant expression of meso-endodermal markers already at the undifferentiated state (Adamo et al., 2011). Importantly, mice devoid of KDM1A die at E7.5, corresponding to the stage of cardiomyocytes specification and formation of the heart tube (Savolainen et al., 2009). A fine-tuned alternative splicing regulation of *KDM1A* transcripts has been linked to the modulation of KDM1A function during development of the nervous system (Zibetti et al., 2010). We therefore sought to investigate how *KDM1A* alternative splicing is regulated during cardiogenesis. We first determined the KDM1A isoforms expressed in hESCs and how their expression is modulated

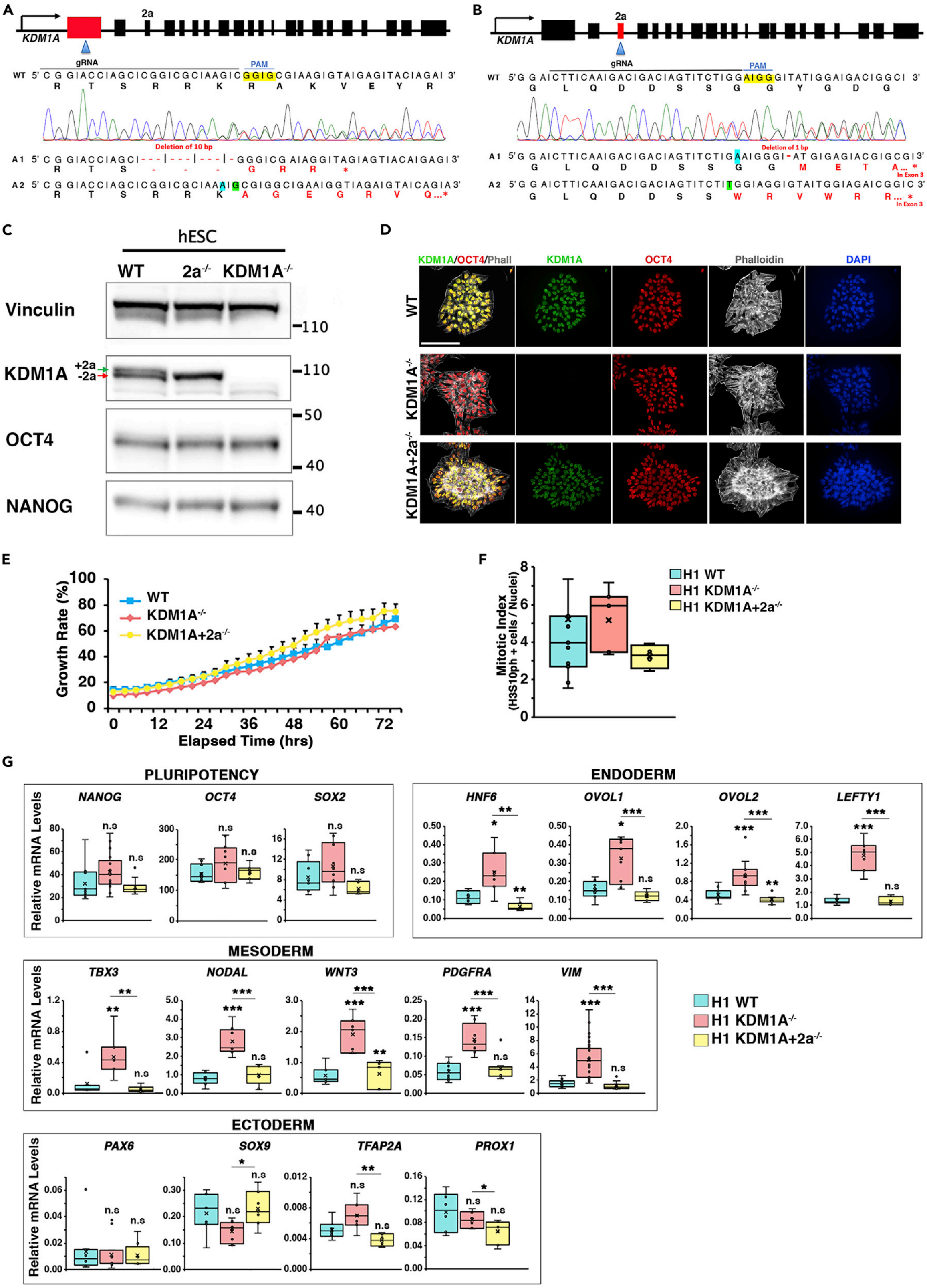
A
B
KDM1A
2a
gRNA
PAM
Deletion of 10 bp
Deletion of 1 bp
In Exon 3
WT
A1
A2
C
hESC
WT
2a-/-
KDM1A-/-
Vinculin
KDM1A
+2a
-2a
OCT4
NANOG
110
50
40
D
KDM1A/OCT4/Phall
KDM1A
OCT4
Phalloidin
DAPI
WT
KDM1A-/-
KDM1A+2a-/-
E
Growth Rate (%)
Elapsed Time (hrs)
WT
KDM1A-/-
KDM1A+2a-/-
F
Mitotic Index (H3S10ph + cells / Nuclei)
H1 WT
H1 KDM1A-/-
H1 KDM1A+2a-/-
G
PLURIPOTENCY
NANOG
OCT4
SOX2
ENDODERM
HNF6
OVOL1
OVOL2
LEFTY1
MESODERM
TBX3
NODAL
WNT3
PDGFRA
VIM
ECTODERM
PAX6
SOX9
TFAP2A
PROX1
Relative mRNA Levels
n.s
*
**
***
H1 WT
H1 KDM1A-/-
H1 KDM1A+2a-/-

Figure 2. CRISPR-Cas9-mediated generation of KDM1A$^{-/-}$ and KDM1A+2a$^{-/-}$ hESCs

(A and B) Scheme of CRISPR approach to generate hESCs carrying nonsense mutations in both *KDM1A* alleles. Red rectangles indicate the exons targeted by the specific gRNA used to direct CRISPR-Cas9gRNA (blue arrows).

(C)Western blot analysis shows the presence of two KDM1A isoforms indicated by green (upper band, KDM1A+2a) and red arrows (lower band, ubKDM1A), respectively in H1.

(D) Immunofluorescence images of H1 hESCs stained for the indicated antibodies. Scale bar, 100 μm.

(E) Proliferation rate is measured as the area occupied by the cells (%) over time (hours). Movies were recorded at 1.5 h/frame for 72 h. Each point is the mean ± STD of cell areas from four different fields from three independent experiments.

(F) Bar plots showing the mitotic index. The score was calculated by dividing the number of H3S10ph-positive cells by the number of positive nuclei stained with DAPI. At least 1200 cells were scored from two independent experiments. Purple dots show the average score from each analyzed field.

(G) mRNA levels of lineage-specific markers analyzed by Taqman assays and normalized to the internal control *TBP*.

N = 5–10 independent experiments, $^*p> 0.05$, $^{**}p> 0.01$, $^{***}p> 0.001$ (Student's *t* test); n.s, not significant. See also Figure S2.

during *in vitro* cardiac cells differentiation. Analyzing transcriptomic data obtained from undifferentiated H1-hESCs, we excluded the presence of *KDM1A* transcripts containing the neuro-specific alternatively spliced E8a, while we detected the ubiquitous isoforms with the E2a inclusion (hereafter KDM1A+2a) and without (hereafter ubKDM1A) (Figures 1A, 1B, and S1A). To precisely quantify the relative expression of the two ubiquitous isoforms, we relied on TaqMan probes specifically recognizing the exon junctions across exons 2-3 and exons 2-2a to detect the inclusion or exclusion of the E2a in *KDM1A* transcripts, respectively. Both variants are also detectable at the protein level as a duplet band through western blot analysis (Figure S1B). Next, we investigated the potential dynamic regulation of the relative expression of KDM1A+2a and ubKDM1A during cardiac specification. To this end, we performed a stepwise planar differentiation experiment, leading to mesodermal precursors, cardiac progenitors and beating cardiomyocytes (Liu et al., 2017) (Figure S1C). This differentiation method yields a relatively heterogeneous population of cardiac cells displaying spontaneous contractions by day 14–18 of differentiation and expressing key cardiomyocyte markers (Figure S1D). Intriguingly, we found that the relative expression of the two isoforms varies over time. Although at the pluripotent stage, the canonical variant ubKDM1A is predominant and expressed about two folds Vs. KDM1A+2a, at day 18 of differentiation, the KDM1A+2a isoform represents about 50% of the total KDM1A at both transcript and protein levels (Figures 1C, 1D, S1E, and S1F). Next, we analyzed the inclusion of E2a in the transcript of mouse and human during heart development. In mice, the E2a inclusion is subjected to dynamic fluctuation in a defined time window. *Kdm1a+2a* levels significantly decrease at the embryonic stage E12.5 and peak during the last day of fetal development (E19.5) and the first day of the postnatal life (P2, Figures 1E–1G). Remarkably, the overall protein levels of KDM1A significantly decrease during heart development. The first reduction of KDM1A is observed at E19.5, followed by a pronounced drop at postnatal life P60 (Figures 1F and 1G), thus highlighting the crucial importance of KDM1A during mice cardiogenesis. The transcriptomic analysis of the human fetal heart at different gestational week ages (GWA) (Pervolaraki et al., 2018) revealed that the isoform including the E2a, but not the one containing the E8a, is detectable in the analyzed stages (Figures S1G and S1H). Moreover, while the mRNA expression of *KDM1A+2a* is stable, the *ubKDM1A* transcript levels significantly drop (about 40%) from 9WGA to 12WGA (Figure 1H). Notably, at 12WGA the ratio of E2a versus ubKDM1A expression increases up to 20% (Figure 1I). These data indicate that the expression of KDM1A isoforms is dynamically regulated during human and rodents heart development, and during cardiac differentiation *in vitro*.

KDM1A+2a is dispensable for the maintenance of human pluripotency

Next, we explored the consequences of the perturbation of the transcriptional ratio of the two variants on pluripotency maintenance. For this purpose, we used a CRISPR/Cas9-mediated approach to generate H1 hESCs genetically depleted for both KDM1A variants (KDM1A$^{-/-}$) or exclusively devoid of KDM1A+2a isoform (KDM1A+2a$^{-/-}$). We designed a gRNA recognizing Exon1 to simultaneously target all variants to generate the KDM1A$^{-/-}$ H1 cells and a gRNA recognizing E2a to exclusively knockout (KO) the KDM1A+2a isoform. We selected and validated two KO clones resulting from frameshift mutations on both alleles for each gRNA (Figures 2A, 2B, S2A, and S2B). RNA expression, immunostaining, and western blot analysis for KDM1A confirmed lower transcriptional levels compared to wild-type (WT) H1 cells and the absence of one or both protein variants in KDM1A+2a$^{-/-}$ and KDM1A$^{-/-}$, respectively (Figures 2C, 2D, S2C, and S2D). Notably, karyotype analysis showed a normal chromosome content in all engineered hESC clones (Figure S2E). Interestingly, the deletion of both KDM1A isoforms, but not KDM1A+2a deficiency alone, induces a morphological change in the hESC colonies that appear studded with spike-like cell projections and more spread, compared to control cells, both characteristics of the early transition of pluripotent cells into a

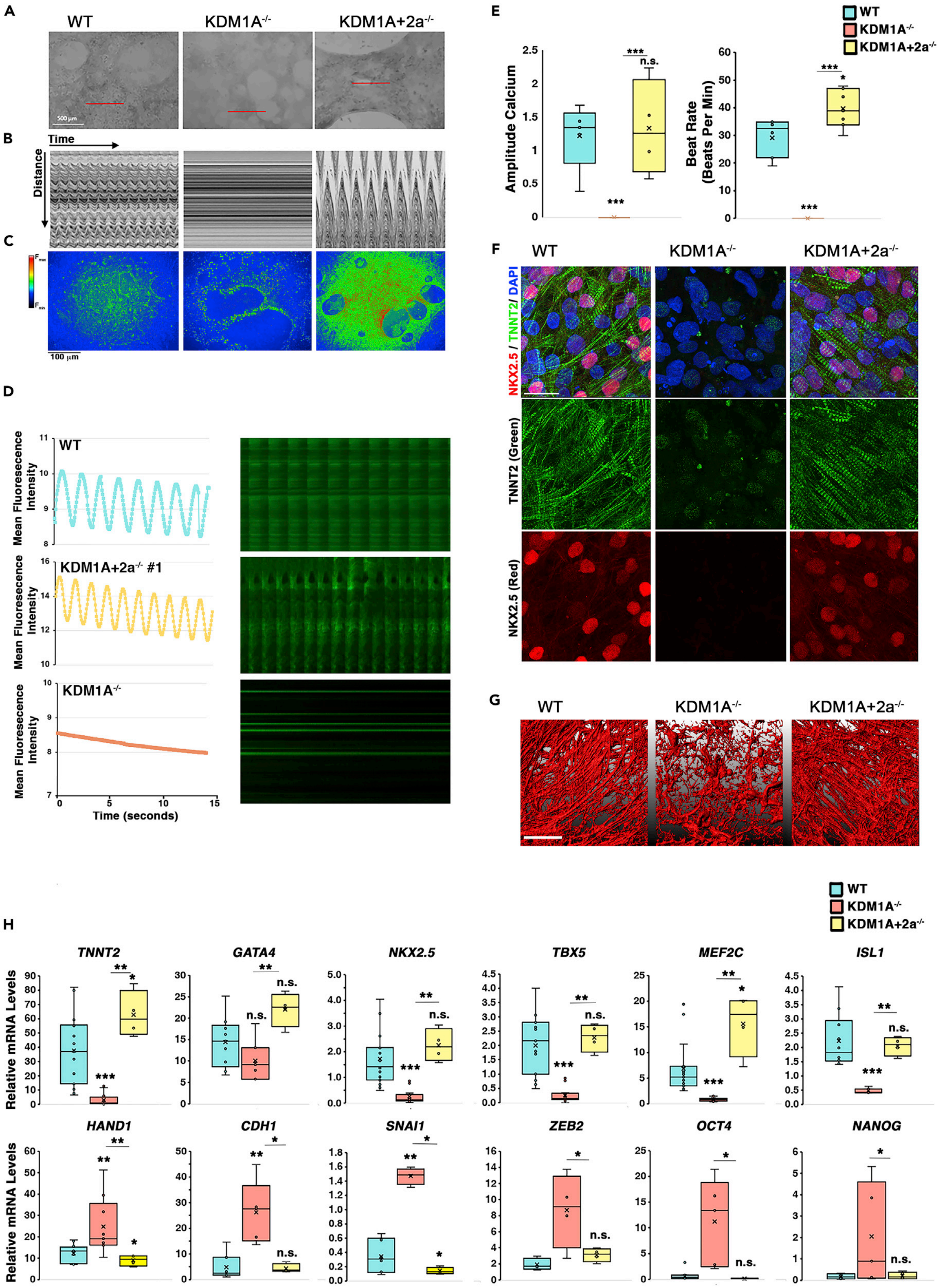
A
WT
KDM1A-/-
KDM1A+2a-/-
500 µm
B
Time
Distance
C
Fmax
Fmin
100 µm
D
Mean Fluorescence Intensity
WT
KDM1A+2a-/- #1
KDM1A-/-
0
5
10
15
Time (seconds)
E
Amplitude Calcium
Beat Rate (Beats Per Min)
WT
KDM1A-/-
KDM1A+2a-/-
***
n.s.
*
F
WT
KDM1A-/-
KDM1A+2a-/-
NKX2.5 / TNNT2/ DAPI
TNNT2 (Green)
NKX2.5 (Red)
G
WT
KDM1A-/-
KDM1A+2a-/-
H
WT
KDM1A-/-
KDM1A+2a-/-
Relative mRNA Levels
TNNT2
GATA4
NKX2.5
TBX5
MEF2C
ISL1
HAND1
CDH1
SNAI1
ZEB2
OCT4
NANOG
**
***
n.s.
*

Figure 3. KDM1A-null hESCs show defective cardiac differentiation, while the KO of the E2a isoform improves the cardiogenic programming

(A) Frames from video recording of H1 derived-beating cardiomyocytes cells at Day 18 post-differentiation. The red line shows the area selected to plot the kymographs. Scale bar, 500 μm.

(B) Kymographs were generated by plotting the time (30 s) along the x axis and distance along the y axis. The oscillatory pattern represents the contraction wave generated by beating cardiomyocytes.

(C) Heatmap showing the intensity of Ca^{2+} transients in each cell line loaded with Fluo-4-AM. Scale bar, 100 μm.

(D) Fifteen seconds imaging recording of Ca^{2+} sparks in each genotype (left), obtained from the one representative kymograph (right).

(E) Box Plots showing calcium amplitude (left) and beat rate (right) during contraction of WT, KDM1A$^{-/-}$ and KDM1A+2a$^{-/-}$ beating cardiomyocytes. N = 4-5 fields from two-three independent experiments. One-way ANOVA, postHoc Tukey HSD test (*$p < 0.05$, ***$p < 0.001$, n.s. = not significant, referred to WT cells).

(F) Immunofluorescence images of hESC-derived cardiac cells at Day 18 of differentiation. Scale bar, 20 μm.

(G) Confocal microscopy Z-stack reconstructed bundles of actin fibers stained with phalloidin. Scale bar, 20 μm.

(H) Expression of cardiac markers in WT, KDM1A$^{-/-}$ and KDM1A+2a$^{-/-}$ cardiac cells analyzed by Taqman assay at Day 18.

Box plots show n = 15–7 independent experiments normalized to *TbP*. n.s. = not significant, *$p > 0.05$, **$p > 0.01$ (Student's *t* test). See also Figure S3 and Videos S1 and S2.

differentiating state. On the other hand, KDM1A+2a$^{-/-}$ cells maintained a compact colony geometry, similarly to WT cells (Figure S2F). We meticulously characterized the derived knockout clones assessing: (1) the growth curve, through live imaging analysis (Figure 2E); (2) the mitotic index, using H3 serine 10 staining (Figure 2F); (3) the apoptotic index through Annexin V and Propidium Iodide staining (Figure S2G); (4) the expression of pluripotency markers at protein and mRNA levels (Figures 2C–2D and 2G); (5) the pluripotency potential by teratoma formation analysis (Figure S2H). Our data demonstrate that the depletion of the E2a containing isoform does not affect any of the assessed stem cells features. On the contrary, KDM1A-null hESCs aberrantly express early developmental genes albeit maintained in undifferentiated conditions (Figure 2G), in agreement with previous data obtained in KDM1A knockdown hESCs (Adamo et al., 2011). Notably, teratomas obtained from KDM1A$^{-/-}$ display prevalent mesodermal and minimal ectodermal components compared to WT cells.

KDM1A depletion impairs the differentiation of hESC into cardiac cells

We then differentiated KDM1A$^{-/-}$ and KDM1A+2a$^{-/-}$ hESCs into cardiac cells. To perform cardiac differentiation, we relied on a 2D *in vitro* chemically defined protocol (Liu et al., 2017) (Figure S1C) that allows the generation of beating cells expressing multiple cardiomyocytes markers such as Myocyte Enhancer Factor 2C (*MEF2C)*, ISL LIM homeobox 1 (*ISL1)*, T-Box Transcription Factor 5 (*TBX5*), NK2 homeobox 5 (*NKX2.5*), and troponin T type 2 (*TNNT2)* (Figure S1D). Strikingly, cardiac cells derived from KDM1A$^{-/-}$ hESC do not exhibit any sign of spontaneous beating activity (Figures 3 and S3). Notably, the lack of beating features in KDM1A$^{-/-}$ cardiac cells is not accompanied by increased cell death (Figures S3E–S3F), a phenomenon previously reported to occur during differentiation of mouse KDM1A$^{-/-}$ ESCs (Foster et al., 2010; Wang et al., 2008; Whyte et al., 2013). The kymograph analyses of the oscillatory waves confirmed that KDM1A$^{-/-}$ cells display a flat pattern and are virtually static. Conversely, KDM1A+2a$^{-/-}$ cardiac cells are characterized by waves of contraction with a significantly larger amplitude than control cells (Figures 3A, 3B, and S3A; Video S1). We reasoned that the lack of spontaneous contraction in KDM1A$^{-/-}$ cells could result from a defect of Ca^{2+} ions release during excitation-contraction coupling. We, therefore, measured calcium sparks using Fluo-4-AM calcium live imaging in WT, KDM1A$^{-/-}$, and KDM1A+2a$^{-/-}$ cardiac cells. In KDM1A null cells, we observed static intracellular calcium-positive structures in the absence of kinetic activity and calcium transmission. On the other hand, KDM1A+2a$^{-/-}$ cultures showed a significantly higher width of calcium flux and contractile synchronicity than WT cardiac cells (Figures 3C–3E, S3B, and S3C; Video S2). Consistently with the macroscopic observations, immunofluorescent staining for the cardiomyocyte markers *NKX2.5* and *TNNT2* revealed expression of both markers in WT and KDM1A+2a$^{-/-}$, but not in KDM1A$^{-/-}$ cells (Figure 3F). In addition, high-resolution microscopy analysis highlighted a complete disruption of the actin bundle network in KDM1A$^{-/-}$ cardiac cells, suggesting that the lack of KDM1A also impacts the proper assembly of the cytoskeletal machinery (Figures 3G and S3D). Accordingly, the mRNA levels of the cardiomyogenic markers *TNNT2*, GATA-binding protein 4 (*GATA4*), *NKX2.5*, *TBX5*, *MEF2C*, and *ISL1* are lowly expressed in KDM1A$^{-/-}$ cells. An intriguing exception is the heart and neural crest derivatives expressed 1 (*HAND1)*, whose transcript levels are increased in KDM1A$^{-/-}$ cardiac cells compared to control cells (Figure 3H). *HAND1* is a transcriptional repressor playing an essential role in cardiac morphogenesis (Firulli et al., 1998; Riley et al., 1998) that was previously identified upregulated in KDM1A-deficient mouse ES cells (Macfarlan et al., 2011). An additional observation is the aberrant expression of the key epithelial-mesenchymal transition (EMT) markers Cadherin-1 (*CDH1*), Snail family transcriptional repressor 1 (*SNAI1*), and E-box-binding homeobox 2 (*ZEB2)* and the residual expression of the

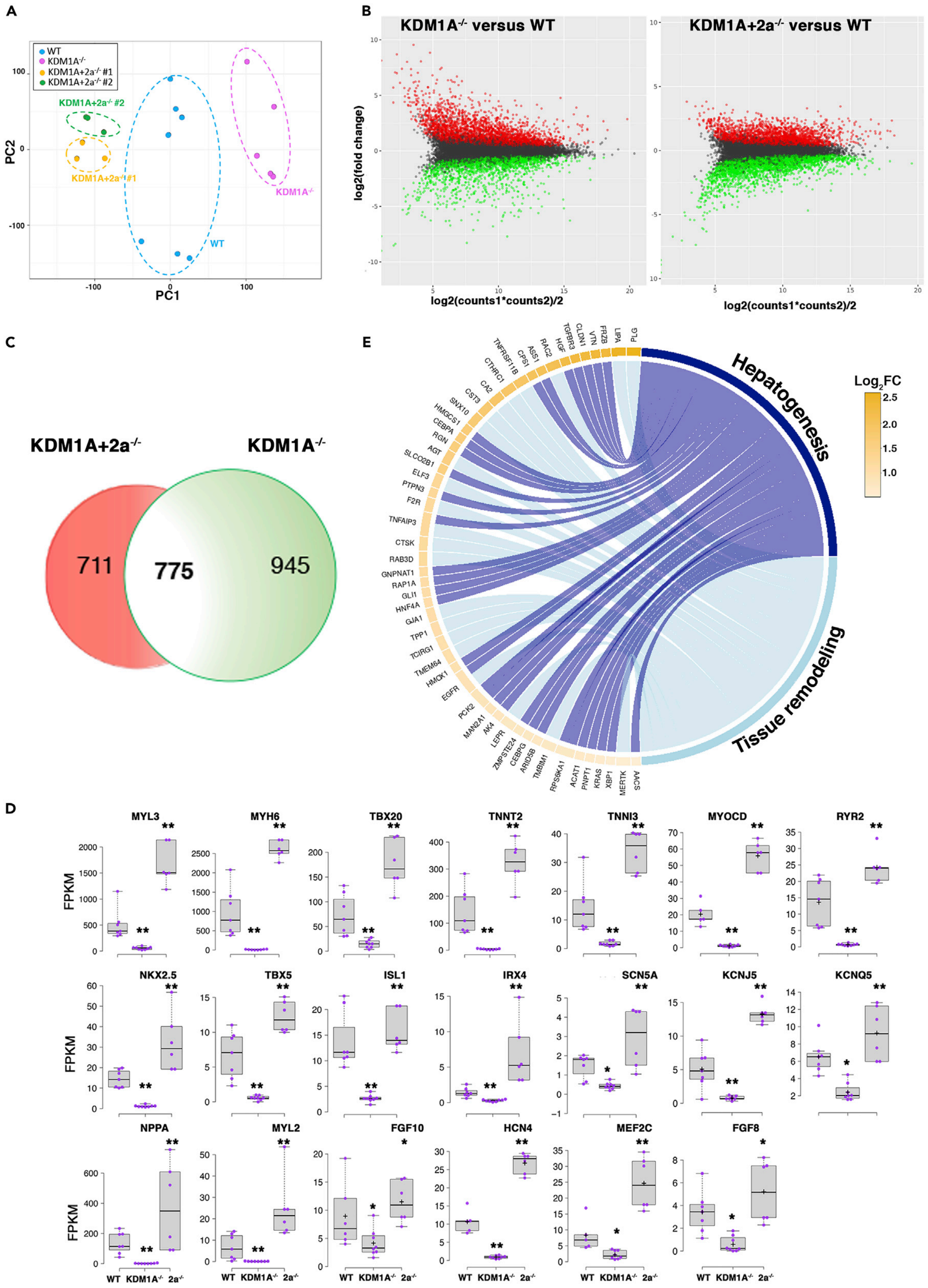
A
WT
KDM1A-/-
KDM1A+2a-/- #1
KDM1A+2a-/- #2
KDM1A+2a-/- #2
KDM1A+2a-/- #1
WT
KDM1A-/-
PC1
PC2
B
KDM1A-/- versus WT
KDM1A+2a-/- versus WT
log2(fold change)
log2(counts1*counts2)/2
C
KDM1A+2a-/-
KDM1A-/-
711
775
945
E
Hepatogenesis
Tissue remodeling
Log2FC
2.5
2.0
1.5
1.0
PLG
LIPA
FRZB
VTN
CLDN1
TGFBR3
HGF
RAC2
ASS1
CPS1
TNFRSF11B
CTHRC1
CA2
CST3
SNX10
HMGCS1
CEBPA
RGN
AGT
SLCO2B1
ELF3
PTPN3
F2R
TNFAIP3
CTSK
RAB3D
GNPNAT1
RAP1A
GLI1
HNF4A
GJA1
TPP1
TCIRG1
TMEM64
HMOX1
EGFR
PCK2
MAN2A1
AK4
LEPR
ZMPSTE24
CEBPG
ARID5B
TMBIM1
RPS6KA1
ACAT1
PNPT1
KRAS
XBP1
MERTK
AACS
D
MYL3
MYH6
TBX20
TNNT2
TNNI3
MYOCD
RYR2
NKX2.5
TBX5
ISL1
IRX4
SCN5A
KCNJ5
KCNQ5
NPPA
MYL2
FGF10
HCN4
MEF2C
FGF8
FPKM
WT
KDM1A-/-
2a-/-
**
*

Figure 4. KDM1A+2a depletion enhances the cardiomyogenic transcriptional program

(A) Principal component analysis of the hESC-derived cardiac cells samples used for the RNA-Seq analysis. Each dot represents an independent biological RNA sample. At least three independent experiments have been conducted for each cell line.

(B) MA plot of differential expressed genes (DEGs) identified in the comparison KMD1A$^{-/-}$ versus WT (left) and KDM1A+2a$^{-/-}$ versus WT (right). Red dots, upregulated genes; green dots, downregulated genes.

(C) Venn diagram showing the common DEGs (775) from the downregulated set in the comparison KDM1A$^{-/-}$ versus WT, and the upregulated set in the comparison KDM1A+2a$^{-/-}$ vs WT.

(D) FPKM gene expression of the most relevant cardiac markers differentially expressed with opposite trend in KDM1A$^{-/-}$ and KDM1A+2a$^{-/-}$ cardiac cells. *$p < 0.05$, **$p < 0.01$ (Student's *t* test). N = 7-6 independent RNA-seq replicates.

(E) Circular plot showing the DEGs involved in the GO term "hepatogenesis" and "tissue remodeling". The $\log_2$FC of each gene is marked by a colored-code rectangle.

See also Figure S4 and Table S5 and Datasets S1, S2, S3, S4, and, S5.

pluripotency markers *OCT4* and *NANOG* in KDM1A$^{-/-}$ differentiated cells (Figure 3H). Significantly, while *HAND1* and *SNAI1* levels are upregulated in cells depleted for both KDM1A variants, they are downregulated in KDM1A+2a$^{-/-}$ compared to control cardiac cells (Figure 3H). Moreover, the increased contractility of KDM1A+2a$^{-/-}$ cardiac cells is coupled with higher *MEF2C* and *TNNT2* expression than WT cells (Figure 3H).

Our results indicate that KDM1A is essential for cardiac differentiation and suggest that a tuned balance between ubKDM1A and KDM1A+2a is determinant for the timely execution of the cardiac transcriptional program.

KDM1A regulates the transcriptional network governing myocardial development

Next, we interrogated the transcriptomes of KDM1A$^{-/-}$ and KDM1A+2a$^{-/-}$ derived cardiac cells (day 14–18) to untangle the gene expression networks regulated by each isoform. We identified 2814 differentially expressed genes (DE-Gs) in the comparison KDM1A$^{-/-}$ Vs. WT and 4032 DE-Gs in KDM1A+2a$^{-/-}$ Vs. WT cells (Figures 4A and 4B and Datasets S1 and S2). The GO analysis in KDM1A$^{-/-}$ highlighted a significant subset of downregulated genes related to cardiac conduction, heart morphogenesis, muscle contraction, potassium ions transport, and mitochondrial respiratory chain. Strikingly, the same gene categories are upregulated in KDM1A+2a$^{-/-}$ cardiac cells (Figures S4A and S4B and Datasets S3 and S4). We then focused on DEGs with opposite expression trends in the two comparisons and we found that 53% of the upregulated genes in KDM1A+2a$^{-/-}$ cells were downregulated in KDM1A$^{-/-}$ cardiac cells (Figure 4C and Dataset S5). Among them were *NKX2.5*, *TBX5*, Myocardin (*MYOCD*), *MEF2C*, and Fibroblast Growth Factor 8/10 (*FGF8/10*), all critical markers of cardiomyocyte specification and Potassium Voltage-Gated Channel Subfamily Q Member 5 (*KCNQ5*), Potassium Inwardly Rectifying Channel Subfamily J Member 5 (*KCNJ5*), Hyperpolarization Activated Cyclic Nucleotide Gated Potassium Channel 4 (*HCN4*), Ryanodine Receptor 2 (*RYR2*), and *TNNT2*, key structural and functional components of cardiac cells(Paige et al., 2012) (Figures 4D and S4A). Within the upregulated gOs in KDM1A$^{-/-}$ cardiac cells, we found processes related to cholesterol, steroid and lipid metabolism (Figures S4B and S4C). A significant number of genes in these categories are early and late markers of hepatic specification or are related to tissue remodeling (Figures 4E, S4D, and S4E). This result could indicate that KDM1A depletion prevents the timely activation of the cardiac transcriptional program and instead leads to the aberrant induction of genes related to the hepatic lineage. Intriguingly, a similar phenomenon has been recently reported in KDM1A$^{-/-}$ mouse satellite cells aberrantly differentiating into brown adipocytes despite being exposed to skeletal muscle differentiating cues (Tosic et al., 2018).

ubKDM1A but not KDM1A+2a rescues cardiac differentiation of KDM1A$^{-/-}$ cells

Previous studies performed in zebrafish Kdm1a-KO models characterized by aberrant hematopoiesis, have shown that the overexpression of any KDM1A isoform is capable of rescuing the hematopoietic-deficient phenotype (Tamaoki et al., 2020). We therefore assessed whether the rescue of either ubiquitous isoform was sufficient to correct the impaired cardiac differentiation of KDM1A$^{-/-}$ cells. To this end, we used undifferentiated KDM1A$^{-/-}$ cells stably transfected with ubKDM1A (KDM1A$^{-/-}$ + ub^{R}) or KDM1A+2a (KDM1A$^{-/-}$+2a^{R}) overexpressing vectors to perform cardiac differentiation experiments (Figures 5A and S5A–S5D). The re-expression of both KDM1A variants was sufficient to rescue the aberrant morphology of KDM1A-null cells and their transcriptional profile in undifferentiated hESCs (Figures S5A and S5E–S5F). Our results indicate that cardiac differentiation, spontaneous beating, and calcium transmission were restored on re-expression of ubKDM1A. Conversely, cells expressing KDM1A+2a exhibited minimal

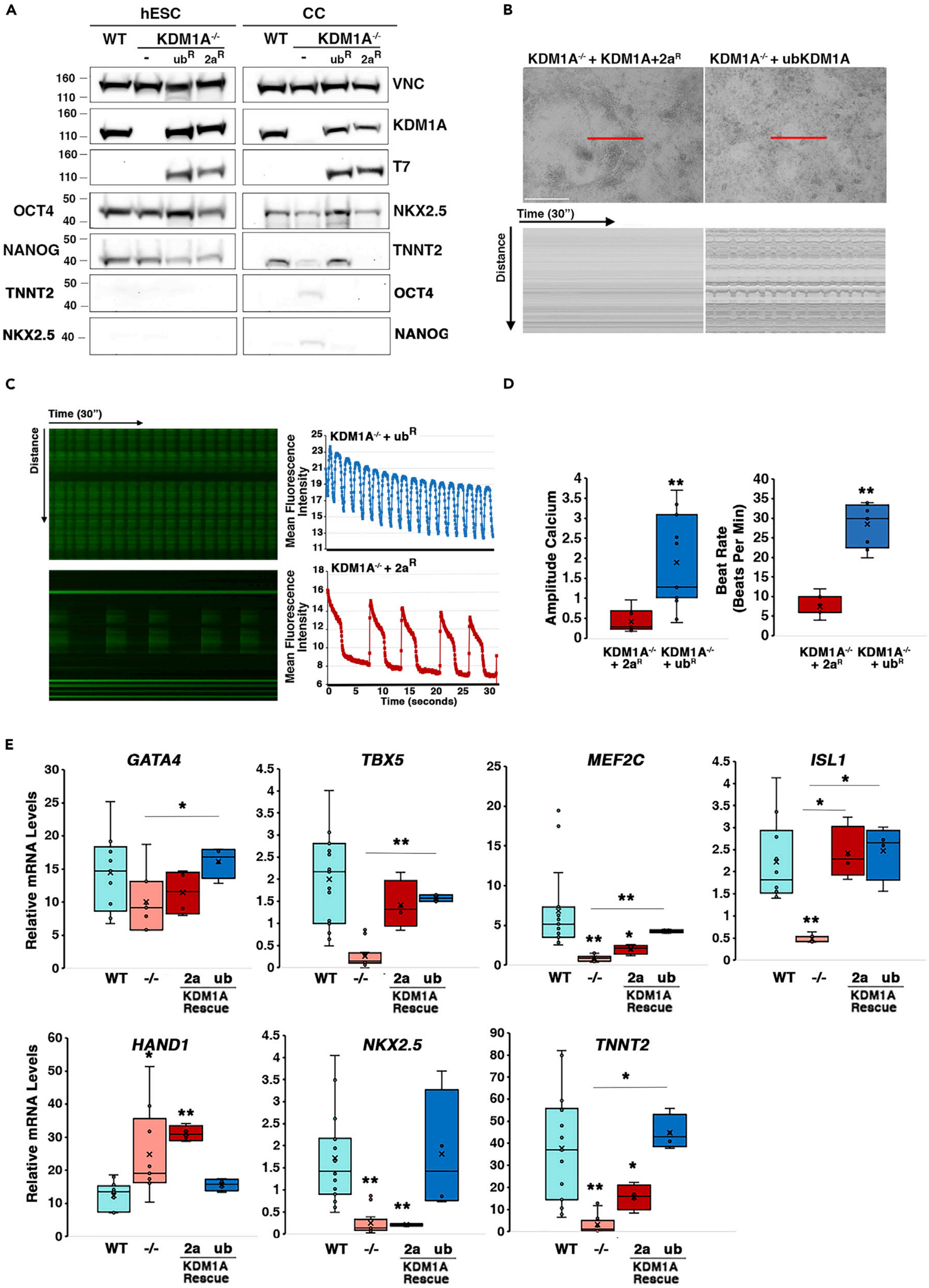
A
hESC
CC
WT
KDM1A-/-
-
ubR
2aR
160
110
50
40
VNC
KDM1A
T7
OCT4
NKX2.5
NANOG
TNNT2
B
KDM1A-/- + KDM1A+2aR
KDM1A-/- + ubKDM1A
Time (30")
Distance
C
Time (30")
Distance
KDM1A-/- + ubR
KDM1A-/- + 2aR
Mean Fluorescence Intensity
Time (seconds)
D
Amplitude Calcium
Beat Rate (Beats Per Min)
KDM1A-/- + 2aR
KDM1A-/- + ubR
**
E
GATA4
TBX5
MEF2C
ISL1
HAND1
NKX2.5
TNNT2
Relative mRNA Levels
WT
-/-
2a
ub
KDM1A Rescue
*
**

Figure 5. ubKDM1A but not KDM1A+2a isoform rescues cardiac differentiation of KDM1A$^{-/-}$ cells

(A)Western blot for KDM1A expression in KDM1A$^{-/-}$ hESCs and cardiac cells (CC) stably rescued with either T7-ubKDM1A or T7-KDM1A+2a isoforms. VNC, vinculin was used as loading control.

(B) Kymographs generated from live imaging acquisition of hESC-derived cardiac cells (30 s).

(C) Kymographs generated from 30 s recording of Ca2+ sparks (left) and corresponding oscillatory pattern of Ca2+ waves (right).

(D) Box Plots showing calcium amplitude (left) and beat rate (right) during contraction of KDM1A$^{-/-}$ cells rescued with either isoform. N=4-5 fields from two-three independent experiments.

(E) Taqman assay for cardiac markers in KDM1A$^{-/-}$ rescued cardiac cells (Day 18).

N = 4–10 independent experiments normalized to *TBP*. *p> 0.05, **p> 0.01 (Student's *t* test). See also Figure S5 and Video S3.

or no rescue (Figure 5B and Video S3). The functional discrepancy between the two variants is evident when comparing the contractility features such as amplitude waves, measured by kymograph analysis, and calcium spikes of the derived cardiac cells (Figures 5C and 5D). Moreover, the transcriptional characterization of the two cell lines showed that ubKDM1A re-expressing cells efficiently rescue the mRNA levels of the cardiac markers *GATA4*, *TBX5*, *ISL1*, *HAND1*, *NKX2.5*, *TNNT2*, and *MEF2C*. On the other hand, cells re-expressing only the E2a variant were unable to rescue the expression of several cardiac genes including *GATA4*, *MEF2C*, *HAND1*, *NKX2.5*, and *TNNT2* (Figure 5E). We then profiled the genomic occupancy of the two isoforms in cardiac cells by performing ChIP-seq experiments on KDM1A-null cardiac cells re-expressing either ubKDM1A or KDM1A+2a. We detected 6068 and 3617 KDM1A binding peaks for KDM1A$^{-/-}$+2a^{R} and KDM1A$^{-/-}$ + ub^{R}, respectively. Intriguingly, the binding profile of both KDM1A variants largely overlaps, with almost 62% of uKDM1A bound genes shared with KDM1A+2a (Figures S6A–S6C and Dataset S6). The distribution of both variants over the genome is significantly enriched at the proximal promoter of target genes (≤3 Kb from the transcription start site, TSS), whereas only a minor portion of KDM1A binding sites (~10%) was found at distal genomic regions (Figure S6D). Notably, we identified multiple KDM1A peaks for both isoforms at the proximal promoter (≤1 Kb from the TSS) and distal regions (≥30 Kb from the TSS) of the *HAND1* locus (Figure S6E). However, even if the binding profile of the two KDM1A isoforms on *HAND1* regulatory regions is comparable, KDM1A$^{-/-}$ and KDM1A+2a$^{-/-}$ cardiac cells demonstrate opposite *HAND1* expression levels (Figures 3H, S6E, and S6F). These results indicate that although the two *KDM1A* variants occupy the same target gene, they regulate its expression with different efficiency. This mechanism could be achieved through a differentially modulated demethylase activity, through a diverging structural role mediated by the recruitment of the two variants in distinct protein complexes, or by the post-translational modification of the alternatively spliced E2a. Next, we analyzed the genomic binding profile of KDM1A on WT derived cardiac cells using an antibody that recognizes both isoforms (ubKDM1A and KDM1A+2a) at different time point during *in vitro* cardiogenesis. Our results demonstrate that KDM1A peaks are enriched at the promoter and, specifically, around the TSS of target genes and, to a less extent, active and poised enhancers (1–2%) at day 2, day 4 and cardiac beating stage (Figures S7A–S7F).

The insertion of E2a does not alter the biochemical and enzymatic properties of KDM1A

The Ex2a sequence is inserted at the start of the SWIRM domain in spatial proximity to the active site of KDM1A (Figures 6A and 6B). This raises a question about the potential influence of the E2a sequence on substrate specificity and demethylation efficiency. Therefore, we studied the enzymatic properties of KDM1A and KDM1A+2a *in vitro* using the recombinant complexes formed by the KDM1A-binding C-terminal portion of human REST corepressor 1 (CoREST1) (residues 305–485) and the full-length human KDM1A, with or without inclusion of the E2a sequence. We first crystallized and solved the structures of both complexes to see if E2a inclusion alters in some way the protein folding in the contiguous regions (Table S1). The electron densities of both structures were indistinguishable from those obtained with the N-terminally deleted KDM1A (Δ123KDM1A) that has been widely employed in previous structural studies (Forneris et al., 2006). Specifically, the N-terminal residues 1–170 of ubKDM1A and 1–191 of KDM1A+2a, including the E2a residues, were not visible in the electron density (Figure 6C). Consistent with these crystallographic data, AlphaFold2 predicts that the N-terminal residues of KDM1A are highly disordered (Tunyasuvunakool et al., 2021). We then tested the H3K4me2 demethylation activity of both complexes using a dimethylK4 peptide substrate comprising the 21 N-terminal residues of H3 ubKDM1A/CoREST and KDM1A+2a/CoREST. The results indicate virtually identical steady-state kinetics parameters, very similar to those featured by the commonly used Δ123KDM1A truncated construct (Table S2) (Forneris et al., 2005). Both complexes were then compared for their sensitivity to variations in the ionic strength of the solution as it has been shown that the electrostatic interaction plays a major role in substrate binding and activity of KDM1A. Again, no differences could be detected for the two complexes (Table S3) (Forneris et al.,

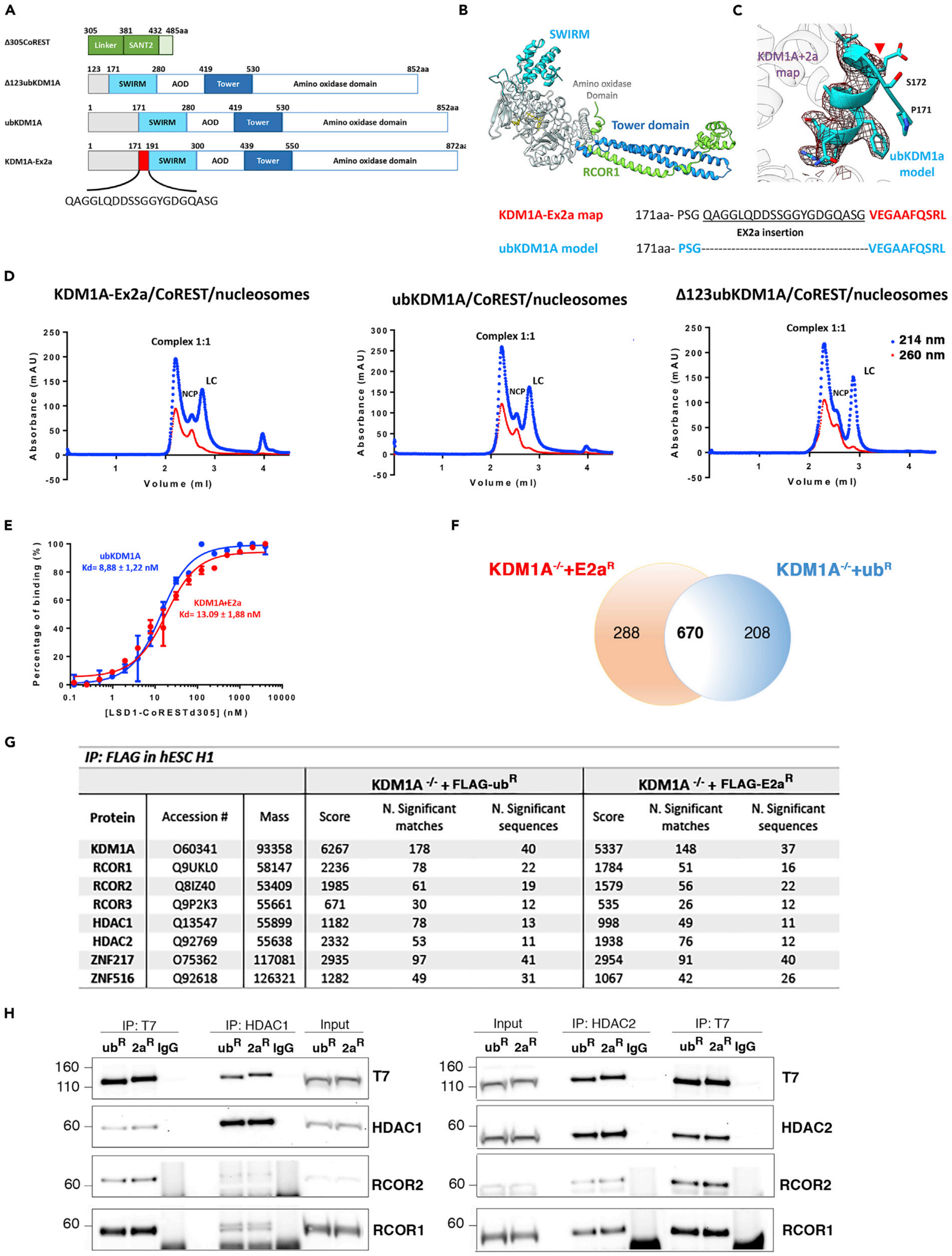

IP: FLAG in hESC H1

			KDM1A -/- + FLAG-ubR			KDM1A -/- + FLAG-E2aR		
Protein	Accession #	Mass	Score	N. Significant matches	N. Significant sequences	Score	N. Significant matches	N. Significant sequences
KDM1A	O60341	93358	6267	178	40	5337	148	37
RCOR1	Q9UKL0	58147	2236	78	22	1784	51	16
RCOR2	Q8IZ40	53409	1985	61	19	1579	56	22
RCOR3	Q9P2K3	55661	671	30	12	535	26	12
HDAC1	Q13547	55899	1182	78	13	998	49	11
HDAC2	Q92769	55638	2332	53	11	1938	76	12
ZNF217	O75362	117081	2935	97	41	2954	91	40
ZNF516	Q92618	126321	1282	49	31	1067	42	26

Figure 6. Biochemical and enzymatic properties of KDM1A isoforms

(A) Schematic of KDM1A and CoREST constructs.

(B) Crystal structure of a KDM1A/CoREST (PDB:2v1d).

(C) Close up view of Pro171, the first ordered residue in the full length KDM1A of the KDM1A+2a/CoREST complex. The arrow outlines the site of E2a insertion after Gly173. The weighted 2Fo-Fc electron density is contoured at 1 σ level. The backbone electron density is interrupted just at the beginning of the region subjected to alternative splicing.

(D) Chromatograms showing the macromolecular species detected after the incubation of KDM1A/CoREST with the nucleosomes containing a propargyl group at the position 4 of H3.

(E) The affinity of KDM1A/CoREST (blue) and KDM1A+2a (red) for a peptide comprising nine N-terminal residues of SNAI1 is evaluated through fluorescence polarization assay.

(F) Venn diagram of the commonly enriched peptides identified by mass spectrometry (MS) in the FLAG-immunoprecipitates.

(G) MS peptide counts identified in KDM1A and IgG co-immunoprecipitates from total lysates of KDM1A$^{-/-}$ hESCs in FLAG-ubKDM1A (FLAG-ub^{R}) or FLAG-KDM1A+2a (FLAG-E2a^{R}).

(H) Western blot analysis of IgG, HDAC1, HDAC2, T7-ubKDM1A and T7-KDM1A+2a from hESC lysates.

See also Tables S1–S3.

2005). ubKDM1A/CoREST and KDM1A+2a/CoREST were finally compared also in the nucleosomal context by incubating them with semisynthetic nucleosomal particles whose H3K4 is chemically modified with a propargylic moiety to form a covalent adduct with the Flavin Adenine Dinucleotide (FAD) of KDM1A as described in (Pilotto et al., 2015). The analysis of the reaction products through a chromatography-based assay showed that both complexes bind to the nucleosome and form a stable KDM1A/CoREST/nucleosome assembly with equal efficiencies (Figure 6D). In summary, E2a inclusion does not alter histone tail binding and nucleosome recognition by KDM1A/CoREST under different experimental conditions.

Next, we probed the effect of E2a inclusion on the binding and inhibition properties of KDM1A. The N-terminal residues of the SNAG transcriptional factors have been shown to bind to the KDM1A active site through a histone mimicry mechanism (Baron et al., 2011). Using fluorescence polarization assay, we found that the binding of a peptide comprising the nine N-terminal residues of SNAI1 is not affected or perturbed by E2a inclusion (Figure 6E). We further performed inhibition experiments using non-covalent (GSK-090) and covalent inhibitors (MC2652, a tranylcypromine analogue). Before substrate addition (10 μM 21 amino acid H3 peptide), the enzyme was incubated with serially diluted inhibitor for 10 min at room temperature. The IC50 values measured for both ubKDM1A/CoREST and KDM1A+2a/CoREST complexes were virtually identical to the IC50 values measured for Δ123KDM1A/CoREST (Table S3). These experiments indicated that the disordered N-terminal residues, with or without E2a, hardly affect the binding properties of the KDM1A active site.

KDM1A+2a and ubKDM1A isoforms are part of the same transcriptional complex

Next, we explored the possibility that the two ubiquitous variants are part of differentially assembled transcriptional complexes. To this aim, we immunoprecipitated either KDM1A+2a or ubKDM1A protein complexes in KDM1A$^{-/-}$ hESCs re-expressing Flag-ub-KDM1A^{R} or Flag-KDM1A + E2a^{R} and performed a mass spectrometry analysis. Our results highlighted a large overlap of binding partners for both variants (about 70%) with high score and significance according to Mascot (Figure 6F and Mendeley Data). Notably, we identified the known interactors of the canonical variant ubKDM1A also in the KDM1A+2a complex, including REST Corepressors (RCORs), Histone deacetylase½2 (HDAC1/2), and the transcription factors zinc-finger protein 217 (ZNF217) and 516 (ZNF516) with similar binding affinity score (Figures 6G and 6H). Focusing on proteins exclusively bound to Flag-ub-KDM1A^{R} or Flag-KDM1A + E2a^{R}, we identified partners with lower number of significant peptides compared with common targets. Moreover, most of the mutually exclusive interactors belong to alternative isoforms or to different subunit of the same protein or complex.

KDM1A catalytic activity is not required for cardiogenesis

Although the biochemical data indicate that the two variants have similar enzymatic properties, we cannot exclude that in the context of the physiological complex assembly *in vivo* they could be differentially modulated. To rule out this possibility and evaluate whether the defective cardiac differentiation of KDM1A-null cells is dependent on the enzymatic activity, we differentiated WT H1 hESCs into cardiac cells in presence of two KDM1A inhibitors, RN-1 and GSK-LSD1 (Cui et al., 2015; McGrath et al., 2016; Mohammad et al., 2015). Our data demonstate that the inhibition of KDM1A doesn't affect the capability of hESCs to differentiate into cardiac cells, nor alter the expression of the canonical RCOR partners (Figures 7A–7C and

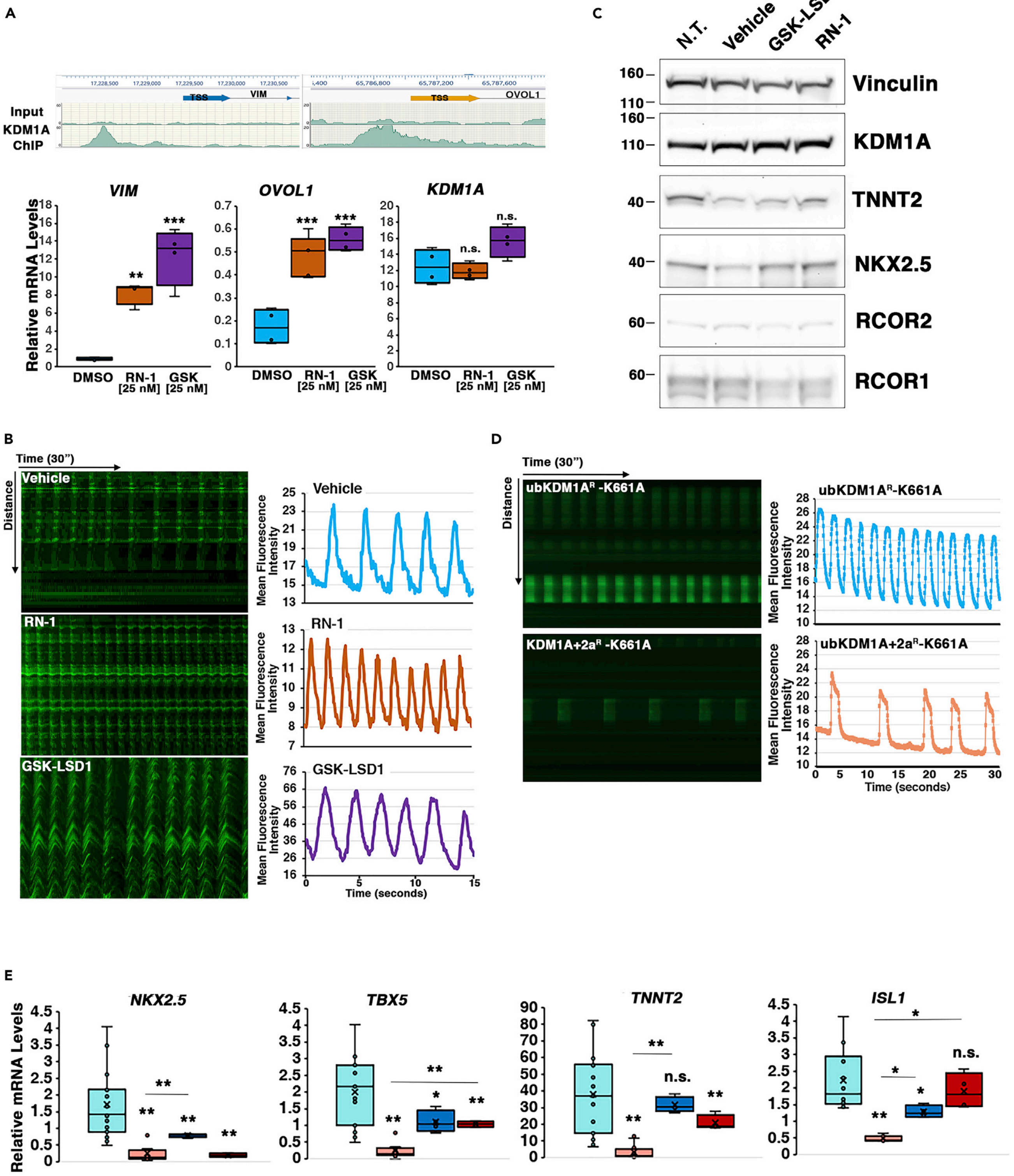

Figure 7. Enzymatic-independent functions of KDM1A during cardiac differentiation

(A) Top: Representative KDM1A ChIP-Seq data showing KDM1A binding at *VIMENTIN* and *OVOL1* loci. TSS, transcription start site; Inp, Input. **Bottom:** Taqman analysis showing the expression of KDM1A targets in hESCs incubated with 25 nM of each KDM1A inhibitor. The inhibition of the histone

Figure 7. *Continued*

demethylase is not altering *KDM1A* mRNA levels. DMSO was used as vehicle. N = 4-5 independent experiments. $^{**}p < 0.01$, $^{***}p < 0.001$ (Student's *t* test), n.s. = not significant.

(B) Kymographs of an imaging recording (30″) of Ca^{2+} sparks in hESCs differentiated in presence of KDM1A inhibitors (left), and corresponding oscillatory pattern (right).

(C)Western blot analysis of cardiac cells differentiated in presence of vehicle (DMSO) or indicated inhibitors. In A-C) RN-1 and GSK-LSD1 inhibitors have been used at the concentration of 25 nM.

(D) Left: kymographs showing Ca^{2+} sparks in KDM1A$^{-/-}$ cardiac cells re-expressing either ubKDM1A^{R}-K661A or KDM1A+2a^{R}-K661A. Right: profile of contraction waves.

(E) Taqman analysis of the indicated transcripts in ubKDM1A^{R}-K661A and KDM1A+2a^{R}-K661A cardiac cells.

N = 4–10 independent experiments normalized to *TBP*. $^{*}p < 0.05$, $^{**}p < 0.01$, $^{***}p < 0.001$ (Student's *t* test), n.s = not significant. See also Figures S6 and S7 and Videos S4 and S5 and Dataset S6.

Video S4). Finally, to exclude that, in inhibited cells, newly synthetized KDM1A could exert a minimal enzymatic function sufficient to sustain cardiac differentiation, we reconstituted KDM1A$^{-/-}$ cells with either ubKDM1A (ubKDM1A^{R}-K661A) or KDM1A+2a (KDM1A+2a^{R}-K661A) catalytically impaired mutants (five-fold decrease in enzymatic activity) (Kim et al., 2020) before differentiation into beating cardiomyocytes. Interestingly, while ubKDM1A^{R}-K661A was able to recapitulate the phenotype of WT cells, the expression of KDM1A+2a^{R}-K661A failed to rescue the contractile phenotype of beating cardiomyocytes (Figure 7D and Video S5). Likewise, the transcriptional signature was only partially rescued by KDM1A+2a^{R}-K661A (Figure 7E). These results demonstrate that the inclusion of Ex2a modulates KDM1A function through an enzymatic and substrate independent mechanism. Altogether these evidences indicate that the catalytic activity of KDM1A is dispensable for the *in vitro* specification of hESCs into myocardial cells and that KDM1A+2a is a functionally inactive isoform of KDM1A.

DISCUSSION

In the present study, we describe the role of KDM1A splicing variants during the differentiation of hESCs into beating cardiomyocytes. We prove that KDM1A isoforms are required to establish the transcriptional program for cardiac development. Gene expression and genomic profiling showed dysregulation of key transcriptional, structural, and functional cardiac markers in KDM1A null-derived cardiac cells. These alterations led to the aberrant differentiation and loss of contraction observed in the cardiac monolayer derived from KDM1A$^{-/-}$ hESCs.

Our findings point to the inefficient shut down of pluripotency markers, the activation of EMT processes, and the aberrant expression of the key regulator of embryonic cardiac development *HAND1* (Firulli et al., 1998; Riley et al., 1998), as leading causes of the defective cardiac differentiation potential of KDM1A$^{-/-}$ hESCs. In addition, KDM1A$^{-/-}$ cardiac cells display improper upregulation of genes related to lipid metabolism. Relevantly, hyperlipidemia is associated with cardiac fibrosis (Ma et al., 2013), and a recent study reported increased cardiac fibrosis in KDM1A$^{-/-}$ cardiac cells *in vivo* (Huo et al., 2021). Therefore, we could speculate that KDM1A ablation promotes cardiac tissue fibrosis by the upregulation of cholesterol and lipid-related pathways. Moreover, a significant subset of upregulated DEGs in KDM1A$^{-/-}$ cardiac cells belongs to hepatic specification and tissue remodeling GO ontologies. Altogether, these results indicate that KDM1A might act as an epigenetic modulator of cell fate decision during cardiac differentiation and regeneration.

Notably, we observed an opposite trend in cardiac cells obtained from hESCs depleted of the E2a (KDM1A+2a$^{-/-}$) compared to KDM1A-KO cells. KDM1A+2a$^{-/-}$ cardiac cells display an increased expression of key cardiac genes and improved contractile phenotypes compared to control cells. Moreover, although the re-expression of ubKDM1A in KDM1A depleted cells leads to an efficient re-establishment of the cardiac transcriptomic signature, the rescue of the E2a variant alone is not sufficient to exert KDM1A functions in the cells. In light of these results, we hypothesize that the E2a isoform acts as a potent modulator of ubKDM1A. The specific depletion of the E2a variant allows better repression of target KDM1A genes (i.e., *HAND1*) and promotes the transcriptional expression of genes governing myocardial development. In favor of the idea that the E2a isoform plays a regulatory role on the ubKDM1A variant, we observed that KDM1A splicing undergoes dynamic fluctuations during mice and human cardiogenesis, and during *in vitro* cardiac differentiation. In mice, the E2a containing transcript significantly decreases, compared to the *ubKdm1a* isoform, at E12.5. This mouse embryonic stage corresponds to the second wave of EMT that, in the heart, contributes to the specification into important cellular subtypes, such as the coronary smooth muscle, cardiac fibroblasts, and connective tissues of the pulmonary and aortic valves (Krainock et al., 2016). Later, *Kdm1a+2a* transcript peaks within E19.5 and the postnatal life (P2), in temporal correlation with a significant transcriptional switch from slow skeletal troponin I (*ssTnI*) to cardiac TnI (*cTnI*) and from cardiac myosin heavy chains isoform β (*β-MHC*) to isoform α (*α-MHC*) (Siedner et al., 2003). In the first trimester of human fetal heart development, the stable expression of the E2a isoform is coupled with a significant drop of *ubKDM1A* mRNA levels. Also, during *in vitro* cardiac specification, the ratio between the two ubiquitous KDM1A isoforms changes at defined time windows, further confirming the physiological importance of maintaining a balanced expression of KDM1A variants during cardiogenesis.

Through genome-wide ChIP-seq analyses, we found that the two KDM1A isoforms are mainly recruited at the promoter of the same genes, therefore excluding the possibility that they act as epigenetic modulators of different pathways. An indisputable example is that although the two isoforms have similar chromatin-binding profile on *HAND1* regulatory regions, they modulate its transcript levels in an opposite fashion. Interestingly, by testing KDM1A occupancy at different stages of *in vitro* cardiac differentiation, we observed a conserved enrichment of KDM1A peaks in the proximity of gene promoters. Scientists are still debating about the localization of KDM1A at promoters rather than at distal enhancers. Previous reports showed KDM1A enrichment at enhancers in undifferentiated and lineage-committed cells (Agarwal et al., 2021; Vinckier et al., 2020; Whyte et al., 2013). Other studies indicated that KDM1A prevalently condenses at the core promoter of target genes (Adamo et al., 2011; Castex et al., 2017; Foster et al., 2010; Laurent et al., 2015). It is plausible that KDM1A is present at both putative enhancers or promoters in association with different protein complexes, as recently proposed (Mak et al., 2021). Enhancer-associated KDM1A could be pivotal to establish and maintain a cell identity program (Agarwal et al., 2021). At the same time, promoter-associated KDM1A can be ready to compensate for transcriptional oscillations that are inherently at the core of the differentiation and maintenance of cells that physiologically perform"excitable" functions, such as neurons and cardiac cells.

We speculated that E2a insertion near the N-terminal disordered region and the SWIRM domain might change the protein conformation or function. In this regard, previous work demonstrated that the overexpressed E2a isoform decreases the affinity for CoREST (Zibetti et al., 2010). Similarly, two studies revealed that E8a insertion leads to an enzymatic fine-tuning of KDM1A through the formation of alternative protein complexes (Laurent et al., 2015) and that nKDM1A+8a phosphorylated at Threnonine-369 in the mouse brain loses the ability to bind corepressor partners (Toffolo et al., 2014). However, our findings excluded that E2a inclusion might alter KDM1A substrate specificity and enzymatic activity *in vitro* by reshaping the SWIRM domain spatial organization. Also, we observed that ubKDM1A and KDM1A+2a have similar binding affinity for known interactors and do not assemble into alternative protein complexes. A complementary possibility is that the inclusion of E2a modifies the unstructured N-terminal portion of KDM1A, serving as a regulatory platform for post-translational regulatory modifications. This hypothesis is coherent with recent works demonstrating that the N-terminal region of KDM1A is subjected to several post-translational changes. For example, the Lysine-114 residue is actively methylated by the Euchromatic Histone Lysine Methyltransferase 2 (EHMT2) and demethylated by the chromodomain-helicase (CHD1) (Metzger et al., 2016). Moreover, phosphorylation at the N-terminal region of KDM1A within Serine-111 by Protein kinase C (PKC) is crucial for its demethylase and EMT-mediated functions (Boulding et al., 2019). KDM1A phosphorylation at Serine-131 and -134 by Cell Kinase 2 isoform a (CK2a) improves the binding to members of the ring finger protein 168 (RNF168 and E3 ubiquitin ligase) and p53-binding protein 1 (53BP1) (Peng et al., 2015). Interestingly, KDM1A harbors canonical (I/L)Q motifs typical for ubiquitination-mediated regulation by F-box proteins (Chen and Mallampalli, 2013). A previous report showed that ubiquitination mediated by Jade Family PHD Finger 2 (Jade-2) controls LSD1 protein levels, and that Jade-2 mediates the regulation of neural-specific KDM1A isoforms (Han et al., 2014). It is tempting to speculate that the stability of alternative KDM1A spliced variants might be regulated with different efficiency and give rise to proteins with diverse biological effectiveness.

Overall, our study demonstrates that the expression levels of ubKDM1A and KDM1A+2a are finely regulated during cardiogenesis both *in vitro* and *in vivo* and that KDM1A splicing variants are critical modulators of the *in vitro* cardiogenic program.

Moreover, we demonstrate that the full catalytic activity of KDM1A is dispensable for cardiac development based on rescue experiments with the enzymatic-deficient KDM1A isoforms (K661A) and blunting KDM1A activity with enzymatic inhibitors (GSK-LSD1 and RN-1). Previously, KDM1A has been shown to act through its demethylase activity as a potent epigenetic regulator in various biological functions (Adamo et al., 2011;

Choi et al., 2010; Laurent et al., 2015; Maiques-Diaz and Somervaille, 2016; Whyte et al., 2013). However, more recently, a plethora of enzymatic-independent KDM1A functions have been described, and it is emerging that KDM1A scaffolding properties finely regulate the recruitment of other proteins to chromatin (Carnesecchi et al., 2017; Nam et al., 2014; Ravasio et al., 2020; Sehrawat et al., 2018; Tamaoki et al., 2020; Vinyard et al., 2019).

Here, we propose an unprecedented mechanism of cardiac transcriptomic regulation mediated by the auto-regulatory functions of KDM1A isoforms. In the heart, in fact, the inclusion of the E2a seems to act as a fine-tuner of the powerful ubKDM1A. These findings open the road for new lines of investigation on enzymatic-independent functions for KDM1A and its regulatory mechanisms during cardiac development that could involve protein stability or changes in nucleosomal/DNA recognition and docking properties. Moreover, our work highlights an exciting original role for KDM1A isoforms that may significantly impact regenerative medicine. Specifically, the derivation of inhibitors targeting KDM1A+2a could be implemented to enhance the differentiation of hESC-derived cardiac cells, which could serve as an inexhaustible source of transplantable cells.

LIMITATIONS OF THE STUDY

KDM1A is a multifaced epigenetic factor for which enzymatic and non-enzymatic roles have been so far described. Here, we highlighted the non-enzymatic role played by KDM1A during cardiogenesis. A limitation of our study is that we cannot exclude the possibility that the enzymatic activity of KDM1A could be required to fine-tune the expression of a subset of targets not identified by our analyses. Future experiments will be aimed at addressing this open question. In addition, it would have been interesting to study the expression of ubKDM1A and KDM1A+2a during the earliest stages of mouse embryo development (up to E9.0). However, the reduced size of the embryos before E9.5 prevented the execution of this analysis.

STAR★METHODS

Detailed methods are provided in the online version of this paper and include the following:

- KEY RESOURCES TABLE
- RESOURCE AVAILABILITY
  - Lead contact
  - Materials availability
  - Data and code availability
- EXPERIMENTAL MODEL AND SUBJECT DETAILS
- METHOD DETAILS
  - hESC culture and cardiac differentiation
  - CRISPR-Cas9 mediated genome editing of the KDM1A gene
  - Plasmids and constructs
  - Plasmid stable transfection
  - Total RNA extraction from mice heart tissues
  - Exon inclusion frequency by relative quantity fluorescent RT-PCR
  - Protein extraction from embryonic and postnatal mice hearts
  - Teratoma assays
  - Karyotype analysis
  - Annexin-V apoptotic assay and FACS analysis
  - Immunofluorescence and microscopy acquisition
  - Live imaging
  - Calcium live staining and kymograph analysis of beating cardiomyocytes
  - Scanning electron microscopy (SEM) sample preparation and imaging
  - Co-immunoprecipitation assay
  - Western blotting
  - Mass spectrometry
  - RNA isolation, cDNA preparation, and reverse-transcription (RT)-PCR
  - Expression, purification, and crystallization
  - Activity toward peptides
  - Activity toward semisynthetic nucleosomes

  - ○ Enzyme inhibition
  - ○ SNAI1 binding
  - ○ RNA-seq library preparation and sequencing
  - ○ RNA-seq data profiling
  - ○ ChIP-sequencing libraries
  - ○ ChIP-sequencing analysis
  - ○ Splicing variant analysis of human fetal cardiac samples
- QUANTIFICATION AND STATISTICAL ANALYSIS

SUPPLEMENTAL INFORMATION

Supplemental information can be found online at https://doi.org/10.1016/j.isci.2022.104665.

ACKNOWLEDGMENTS

We thank Francesco Rusconi for performing the collection of the embryonal heart tissues. We thank Carol Buitrago-López for her support with graphical abstract preparation. We thank the genomic unit of the KAUST BioCoreLab for technical support with RNA-Seq libraries preparation. We thank the KAUST imaging and characterization facility and ARCL animal facility for support with image acquisition and teratoma formation assays. We thank Sudharshan Elangovan for the generation of the pTP6-Flag-ubKDM1A, pTP6-Flag-KDM1A+2a, pTP6-Flag-ubKDM1A-K661A, and pTP6-Flag-KDM1A+2a-K661A constructs. The two KDM1A inhibitors GSK-090 and MC2652 tranylcypromine were a kind gift of Prof. Antonello Mai, University''"La Sapienza, Rome''" This work was funded by baseline funding (BAS 1077-01-01) to A.A. and by Competitive Research Fund (CRG URF/1/4012) to A.A., A.M., and E.B.

AUTHOR CONTRIBUTIONS

A.V. generated all cell lines, performed the differentiation experiments, live imaging acquisitions, and time-lapse analysis, carried out the iPs, mass spectrometry, and RNA-seq analysis. G.R.C. performed most of the experiments required by reviewers, including differentiation experiments, western blots, and apoptosis analyses at FACS. R.P. optimized the differentiation protocol into cardiac cells, performed real-time PCR, ChIP experiments, and generated ChIP-seq and RNA-seq libraries. J.C. and A.M. performed the *in vitro* biochemical analysis and interpreted the results. A.S.-V. analyzed the ChIP-seq data and assisted with generating the RNA-seq analysis. K.C.L. performed the transcriptomic analysis on the human heart fetal RNA-seq. C.F. and E.B. collected heart mice samples and performed real-time PCR on KDM1A isoforms. E.F. carried out the teratoma formation assays and the cell preparation for karyotype analysis. F.M. performed real-time PCR and RNA-seq libraries. M.A. performed real-time PCRs. E.S. and A.F. performed the S.E.M. acquisitions. F.G. and N.M. trained V.A. for the generation of the genome-edited cell lines. A.V., J.C., A.M., E.B., and A.A. interpreted the results and wrote the manuscript. A.A. designed the study, conceived and supervised the project.

DECLARATION OF INTERESTS

The authors declare no competing interests.

Received: January 18, 2022
Revised: May 31, 2022
Accepted: June 17, 2022
Published: July 15, 2022

REFERENCES

Adamo, A., Atashpaz, S., Germain, P.-L., Zanella, M., D'Agostino, G., Albertin, V., Chenoweth, J., Micale, L., Fusco, C., Unger, C., et al. (2014). 7q11.23 dosage-dependent dysregulation in human pluripotent stem cells affects transcriptional programs in disease-relevant lineages. Nat. Genet. *47*, 132–141. https://doi.org/10.1038/ng.3169.

Adamo, A., Sesé, B., Boue, S., Castaño, J., Paramonov, I., Barrero, M.J., and Belmonte, J.C.I. (2011). LSD1 regulates the balance between self-renewal and differentiation in human embryonic stem cells. Nat. Cell Biol. *13*, 652–659. https://doi.org/10.1038/ncb2246.

Agarwal, S., Bonefas, K.M., Garay, P.M., Brookes, E., Murata-Nakamura, Y., Porter, R.S., Macfarlan, T.S., Ren, B., and Iwase, S. (2021). KDM1A maintains genome-wide homeostasis of transcriptional enhancers. Genome Res. *31*, 186–197. https://doi.org/10.1101/gr.234559.118.

Andrés-Delgado, L., and Mercader, N. (2016). Interplay between cardiac function and heart development. Biochim. Biophys. Acta. *1863*, 1707–1716. https://doi.org/10.1016/j.bbamcr.2016.03.004.

Baron, R., Binda, C., Tortorici, M., McCammon, J.A., and Mattevi, A. (2011). Molecular mimicry and ligand recognition in binding and catalysis by the histone demethylase LSD1-CoREST complex.

Structure *19*, 212–220. https://doi.org/10.1016/j.str.2011.01.001.

Boulding, T., McCuaig, R.D., Tan, A., Hardy, K., Wu, F., Dunn, J., Kalimutho, M., Sutton, C.R., Forwood, J.K., Bert, A.G., et al. (2019). Author Correction: LSD1 activation promotes inducible EMT programs and modulates the tumour microenvironment in breast cancer. Sci. Rep. *9*, 18771. https://doi.org/10.1038/s41598-019-55020-1.

Bushnell, B., Rood, J., and Singer, E. (2017). BBMerge – accurate paired shotgun read merging via overlap. PLoS One *12*, e0185056. https://doi.org/10.1371/journal.pone.0185056.

Carnesecchi, J., Forcet, C., Zhang, L., Tribollet, V., Barenton, B., Boudra, R., Cerutti, C., Billas, I.M.L., Sérandour, A.A., Carroll, J.S., et al. (2017). ERRα induces H3K9 demethylation by LSD1 to promote cell invasion. Proc. Natl. Acad. Sci. USA *114*, 3909–3914. https://doi.org/10.1073/pnas.1614664114.

Castex, J., Willmann, D., Kanouni, T., Arrigoni, L., Li, Y., Friedrich, M., Schleicher, M., Wöhrle, S., Pearson, M., Kraut, N., et al. (2017). Inactivation of Lsd1 triggers senescence in trophoblast stem cells by induction of Sirt4. Cell Death Dis. *8*, e2631. https://doi.org/10.1038/cddis.2017.48.

Chen, B.B., and Mallampalli, R.K. (2013). F-box protein substrate recognition: a new insight. Cell Cycle *12*, 1009–1010. https://doi.org/10.4161/cc.23071.

Choi, J., Jang, H., Kim, H., Kim, S.-T., Cho, E.-J., and Youn, H.-D. (2010). Histone demethylase LSD1 is required to induce skeletal muscle differentiation by regulating myogenic factors. Biochem. Biophys. Res. Commun. *401*, 327–332. https://doi.org/10.1016/j.bbrc.2010.09.014.

Cooper, T.A., and Ordahl, C.P. (1985). A single cardiac troponin T gene generates embryonic and adult isoforms via developmentally regulated alternate splicing. J. Biol. Chem. *260*, 11140–11148. https://doi.org/10.1016/S0021-9258(17)39158-5.

Cui, S., Lim, K.-C., Shi, L., Lee, M., Jearawiriyapaisarn, N., Myers, G., Campbell, A., Harro, D., Iwase, S., Trievel, R.C., et al. (2015). The LSD1 inhibitor RN-1 induces fetal hemoglobin synthesis and reduces disease pathology in sickle cell mice. Blood *126*, 386–396. https://doi.org/10.1182/blood-2015-02-626259.

Da, G., Lenkart, J., Zhao, K., Shiekhattar, R., Cairns, B.R., and Marmorstein, R. (2006). Structure and function of the SWIRM domain, a conserved protein module found in chromatin regulatory complexes. Proc. Natl. Acad. Sci. USA *103*, 2057–2062.

Dobin, A., Davis, C.A., Schlesinger, F., Drenkow, J., Zaleski, C., Jha, S., Batut, P., Chaisson, M., and Gingeras, T.R. (2012). STAR: ultrafast universal RNA-seq aligner. Bioinformatics *29*, 15–21. https://doi.org/10.1093/bioinformatics/bts635.

Epstein, J.A. (2010). Franklin H. Epstein Lecture. Cardiac development and implications for heart disease. N. Engl. J. Med. *363*, 1638–1647. https://doi.org/10.1056/NEJMra1003941.

Fei, Q., Qiu, M., Fan, G., Zhang, B., Wang, Q., Zhang, S., Wang, S., Yang, B., and Zhang, L. (2021). Downregulation of hotair or LSD1 impaired heart regeneration in the neonatal mouse. DNA Cell Biol. *40*, 1177–1184. https://doi.org/10.1089/dna.2021.0095.

Firulli, A.B., McFadden, D.G., Lin, Q., Srivastava, D., and Olson, E.N. (1998). Heart and extra-embryonic mesodermal defects in mouse embryos lacking the bHLH transcription factor Hand1. Nat. Genet. *18*, 266–270. https://doi.org/10.1038/ng0398-266.

Forneris, F., Binda, C., Dall'Aglio, A., Fraaije, M.W., Battaglioli, E., and Mattevi, A. (2006). A highly specific mechanism of histone H3-K4 recognition by histone demethylase LSD1. J. Biol. Chem. *281*, 35289–35295. https://doi.org/10.1074/jbc.M607411200.

Forneris, F., Binda, C., Vanoni, M.A., Mattevi, A., and Battaglioli, E. (2005). Histone demethylation catalysed by LSD1 is a flavin-dependent oxidative process. FEBS Lett. *579*, 2203–2207. https://doi.org/10.1016/j.febslet.2005.03.015.

Foster, C.T., Dovey, O.M., Lezina, L., Luo, J.L., Gant, T.W., Barlev, N., Bradley, A., and Cowley, S.M. (2010). Lysine-specific demethylase 1 regulates the embryonic transcriptome and CoREST stability. Mol. Cell Biol. *30*, 4851–4863. https://doi.org/10.1128/MCB.00521-10.

Gi, W.-T., Haas, J., Sedaghat-Hamedani, F., Kayvanpour, E., Tappu, R., Lehmann, D.H., Shirvani Samani, O., Wisdom, M., Keller, A., Katus, H.A., and Meder, B. (2020). Epigenetic regulation of alternative mRNA splicing in dilated cardiomyopathy. J. Clin. Med. *9*, 1499. https://doi.org/10.3390/jcm9051499.

Giudice, J., Xia, Z., Wang, E.T., Scavuzzo, M.A., Ward, A.J., Kalsotra, A., Wang, W., Wehrens, X.H.T., Burge, C.B., Li, W., and Cooper, T.A. (2014). Alternative splicing regulates vesicular trafficking genes in cardiomyocytes during postnatal heart development. Nat Comms. *5*, 3603. https://doi.org/10.1038/ncomms4603.

Godt, R.E., Fogaça, R., Silva, I.K., and Nosek, T.M. (1993). Contraction of developing avian heart muscle. Comp. Biochem. Physiol. A Comp. Physiol. *105*, 213–218. https://doi.org/10.1016/0300-9629(93)90197-c.

González, F., Zhu, Z., Shi, Z.-D., Lelli, K., Verma, N., Li, Q.V., and Huangfu, D. (2014). An iCRISPR platform for rapid, multiplexable, and inducible genome editing in human pluripotent stem cells. Cell Stem Cell *15*, 215–226. https://doi.org/10.1016/j.stem.2014.05.018.

Han, X., Gui, B., Xiong, C., Zhao, L., Liang, J., Sun, L., Yang, X., Yu, W., Si, W., Yan, R., et al. (2014). Destabilizing LSD1 by jade-2 promotes neurogenesis: an antibraking system in neural development. Mol. Cell *55*, 482–494. https://doi.org/10.1016/j.molcel.2014.06.006.

Hsu, P.D., Lander, E.S., and Zhang, F. (2014). Development and applications of CRISPR-cas9 for genome engineering. Cell *157*, 1262–1278. https://doi.org/10.1016/j.cell.2014.05.010.

Huo, J.-L., Jiao, L., An, Q., Chen, X., Qi, Y., Wei, B., Zheng, Y., Shi, X., Gao, E., Liu, H.-M., et al. (2021). Myofibroblast deficiency of LSD1 alleviates TAC-induced heart failure. Circ. Res. *129*, 400–413. https://doi.org/10.1161/CIRCRESAHA.120.318149.

Kalsotra, A., Xiao, X., Ward, A.J., Castle, J.C., Johnson, J.M., Burge, C.B., and Cooper, T.A. (2008). A postnatal switch of CELF and MBNL proteins reprograms alternative splicing in the developing heart. Proc. Natl. Acad. Sci. USA *105*, 20333–20338. https://doi.org/10.1073/pnas.0809045105.

Kim, S.-A., Zhu, J., Yennawar, N., Eek, P., and Tan, S. (2020). Crystal structure of the LSD1/CoREST histone demethylase bound to its nucleosome substrate. Mol. Cell *78*, 903–914.e4. https://doi.org/10.1016/j.molcel.2020.04.019.

Krainock, M., Toubat, O., Danopoulos, S., Beckham, A., Warburton, D., and Kim, R. (2016). Epicardial epithelial-to-mesenchymal transition in heart development and disease. J. Clin. Med. *5*, 27. https://doi.org/10.3390/jcm5020027.

Langmead, B., Wilks, C., Antonescu, V., and Charles, R. (2019). Scaling read aligners to hundreds of threads on general-purpose processors. Bioinformatics *35*, 421–432. https://doi.org/10.1093/bioinformatics/bty648.

Laurent, B., Ruitu, L., Murn, J., Hempel, K., Ferrao, R., Xiang, Y., Liu, S., Garcia, B.A., Wu, H., Wu, F., et al. (2015). A specific LSD1/KDM1A isoform regulates neuronal differentiation through H3K9 demethylation. Mol. Cell *57*, 957–970. https://doi.org/10.1016/j.molcel.2015.01.010.

Liao, Y., Smyth, G.K., and Shi, W. (2014). featureCounts: an efficient general purpose program for assigning sequence reads to genomic features. Bioinformatics *30*, 923–930. https://doi.org/10.1093/bioinformatics/btt656.

Liu, Q., Jiang, C., Xu, J., Zhao, M.-T., Van Bortle, K., Cheng, X., Wang, G., Chang, H.Y., Wu, J.C., and Snyder, M.P. (2017). Genome-wide temporal profiling of transcriptome and open chromatin of early cardiomyocyte differentiation derived from hiPSCs and hESCs. Circ. Res. *121*, 376–391. https://doi.org/10.1161/CIRCRESAHA.116.310456.

Ma, K.L., Liu, J., Ni, J., Zhang, Y., Lv, L.L., Tang, R.N., Ni, H.F., Ruan, X.Z., and Liu, B.C. (2013). Inflammatory stress exacerbates the progression of cardiac fibrosis in high-fat-fed apolipoprotein E knockout mice via endothelial-mesenchymal transition. Int. J. Med. Sci. *10*, 420–426. https://doi.org/10.7150/ijms.5723.

Macfarlan, T.S., Gifford, W.D., Agarwal, S., Driscoll, S., Lettieri, K., Wang, J., Andrews, S.E., Franco, L., Rosenfeld, M.G., Ren, B., and Pfaff, S.L. (2011). Endogenous retroviruses and neighboring genes are coordinately repressed by LSD1/KDM1A. Genes Dev. *25*, 594–607. https://doi.org/10.1101/gad.2008511.

Maiques-Diaz, A., and Somervaille, T.C. (2016). LSD1: biologic roles and therapeutic targeting. Epigenomics *8*, 1103–1116. https://doi.org/10.2217/epi-2016-0009.

Mak, K.H.-M., Lam, Y.M., and Ng, R.K. (2021). Histone demethylase JMJD2B/KDM4B regulates transcriptional program via distinctive epigenetic targets and protein interactors for the maintenance of trophoblast stem cells. Sci. Rep. *11*, 884. https://doi.org/10.1038/s41598-020-79601-7.

Martin, M. (2011). Cutadapt removes adapter sequences from high-throughput sequencing reads. EMBnet.journal *17*, 10. https://doi.org/10.14806/ej.17.1.200.

McAuliffe, J.J., Gao, L.Z., and Solaro, R.J. (1990). Changes in myofibrillar activation and troponin C Ca2+ binding associated with troponin T isoform switching in developing rabbit heart. Circ. Res. *66*, 1204–1216. https://doi.org/10.1161/01.res.66.5.1204.

McGrath, J.P., Williamson, K.E., Balasubramanian, S., Odate, S., Arora, S., Hatton, C., Edwards, T.M., O'Brien, T., Magnuson, S., Stokoe, D., et al. (2016). Pharmacological inhibition of the histone lysine demethylase KDM1A suppresses the growth of multiple acute myeloid leukemia subtypes. Cancer Res. *76*, 1975–1988. https://doi.org/10.1158/0008-5472.CAN-15-2333.

Meder, B., Haas, J., Sedaghat-Hamedani, F., Kayvanpour, E., Frese, K., Lai, A., Nietsch, R., Scheiner, C., Mester, S., Bordalo, D.M., et al. (2017). Epigenome-wide association study identifies cardiac gene patterning and a novel class of biomarkers for heart failure. Circulation *136*, 1528–1544. https://doi.org/10.1161/CIRCULATIONAHA.117.027355.

Metsalu, T., and Vilo, J. (2015). ClustVis: a web tool for visualizing clustering of multivariate data using Principal Component Analysis and heatmap. Nucleic Acids Res. *43*, W566–W570. https://doi.org/10.1093/nar/gkv468.

Metzger, E., Willmann, D., McMillan, J., Forne, I., Metzger, P., Gerhardt, S., Petroll, K., von Maessenhausen, A., Urban, S., Schott, A.-K., et al. (2016). Assembly of methylated KDM1A and CHD1 drives androgen receptor–dependent transcription and translocation. Nat. Struct. Mol. Biol. *23*, 132–139. https://doi.org/10.1038/nsmb.3153.

Metzger, E., Wissmann, M., Yin, N., Müller, J.M., Schneider, R., Peters, A.H.F.M., Günther, T., Buettner, R., and Schüle, R. (2005). LSD1 demethylates repressive histone marks to promote androgen-receptor-dependent transcription. Nature *437*, 436–439. https://doi.org/10.1038/nature04020.

Mohammad, H.P., Smitheman, K.N., Kamat, C.D., Soong, D., Federowicz, K.E., Van Aller, G.S., Schneck, J.L., Carson, J.D., Liu, Y., Butticello, M., et al. (2015). A DNA hypomethylation signature predicts antitumor activity of LSD1 inhibitors in SCLC. Cancer Cell *28*, 57–69. https://doi.org/10.1016/j.ccell.2015.06.002.

Nam, H.J., Boo, K., Kim, D., Han, D.-H., Choe, H.K., Kim, C.R., Sun, W., Kim, H., Kim, K., Lee, H., et al. (2014). Phosphorylation of LSD1 by PKCα is crucial for circadian rhythmicity and phase resetting. Mol. Cell *53*, 791–805. https://doi.org/10.1016/j.molcel.2014.01.028.

Neagoe, C., Kulke, M., del Monte, F., Gwathmey, J.K., de Tombe, P.P., Hajjar, R.J., and Linke, W.A. (2002). Titin isoform switch in ischemic human heart disease. Circulation *106*, 1333–1341. https://doi.org/10.1161/01.cir.0000029803.93022.93.

Niebel, D., Kirfel, J., Janzen, V., Höller, T., Majores, M., and Gütgemann, I. (2014). Lysine-specific demethylase 1 (LSD1) in hematopoietic and lymphoid neoplasms. Blood *124*, 151–152. https://doi.org/10.1182/blood-2014-04-569525.

Paige, S.L., Thomas, S., Stoick-Cooper, C.L., Wang, H., Maves, L., Sandstrom, R., Pabon, L., Reinecke, H., Pratt, G., Keller, G., et al. (2012). A temporal chromatin signature in human embryonic stem cells identifies regulators of cardiac development. Cell *151*, 221–232. https://doi.org/10.1016/j.cell.2012.08.027.

Peng, B., Wang, J., Hu, Y., Zhao, H., Hou, W., Zhao, H., Wang, H., Liao, J., and Xu, X. (2015). Modulation of LSD1 phosphorylation by CK2/WIP1 regulates RNF168-dependent 53BP1 recruitment in response to DNA damage. Nucleic Acids Res. *43*, 5936–5947. https://doi.org/10.1093/nar/gkv528.

Pervolaraki, E., Dachtler, J., Anderson, R.A., and Holden, A.V. (2018). The developmental transcriptome of the human heart. Sci. Rep. *8*, 15362. https://doi.org/10.1038/s41598-018-33837-6.

Pilotto, S., Speranzini, V., Tortorici, M., Durand, D., Fish, A., Valente, S., Forneris, F., Mai, A., Sixma, T.K., Vachette, P., and Mattevi, A. (2015). Interplay among nucleosomal DNA, histone tails, and corepressor CoREST underlies LSD1-mediated H3 demethylation. Proc. Natl. Acad. Sci. USA *112*, 2752–2757. https://doi.org/10.1073/pnas.1419468112.

Pratt, T., Sharp, L., Nichols, J., Price, D.J., and Mason, J.O. (2000). Embryonic stem cells and transgenic mice ubiquitously expressing a tau-tagged green fluorescent protein. Dev. Biol. *228*, 19–28. https://doi.org/10.1006/dbio.2000.9935.

Rau, A., Gallopin, M., Celeux, G., and Jaffrézic, F. (2013). Data-based filtering for replicated high-throughput transcriptome sequencing experiments. Bioinformatics *29*, 2146–2152. https://doi.org/10.1093/bioinformatics/btt350.

Ravasio, R., Ceccacci, E., Nicosia, L., Hosseini, A., Rossi, P.L., Barozzi, I., Fornasari, L., Zuffo, R.D., Valente, S., Fioravanti, R., et al. (2020). Targeting the scaffolding role of LSD1 (KDM1A) poises acute myeloid leukemia cells for retinoic acid-induced differentiation. Sci. Adv. *6*, eaax2746. https://doi.org/10.1126/sciadv.aax2746.

Riley, P., Anson-Cartwight, L., and Cross, J.C. (1998). The Hand1 bHLH transcription factor is essential for placentation and cardiac morphogenesis. Nat. Genet. *18*, 271–275. https://doi.org/10.1038/ng0398-271.

Robinson, M.D., McCarthy, D.J., and Smyth, G.K. (2009). edgeR: a Bioconductor package for differential expression analysis of digital gene expression data. Bioinformatics *26*, 139–140. https://doi.org/10.1093/bioinformatics/btp616.

Rusconi, F., Grillo, B., Ponzoni, L., Bassani, S., Toffolo, E., Paganini, L., Mallei, A., Braida, D., Passafaro, M., Popoli, M., et al. (2016). LSD1 modulates stress-evoked transcription of immediate early genes and emotional behavior. Proc. Natl. Acad. Sci. USA *113*, 3651–3656. https://doi.org/10.1073/pnas.1511974113.

Rusconi, F., Paganini, L., Braida, D., Ponzoni, L., Toffolo, E., Maroli, A., Landsberger, N., Bedogni, F., Turco, E., Pattini, L., et al. (2015). LSD1 neurospecific alternative splicing controls neuronal excitability in mouse models of epilepsy. Cerebr. Cortex *25*, 2729–2740. https://doi.org/10.1093/cercor/bhu070.

Savolainen, S.M., Foley, J.F., and Elmore, S.A. (2009). Histology atlas of the developing mouse heart with emphasis on E11.5 to E18.5. Toxicol. Pathol. *37*, 395–414. https://doi.org/10.1177/0192623309335060.

Schoenauer, R., Emmert, M.Y., Felley, A., Ehler, E., Brokopp, C., Weber, B., Nemir, M., Faggian, G.G., Pedrazzini, T., Falk, V., et al. (2011). EH-myomesin splice isoform is a novel marker for dilated cardiomyopathy. Basic Res. Cardiol. *106*, 233–247. https://doi.org/10.1007/s00395-010-0131-2.

Scotti, M.M., and Swanson, M.S. (2016). RNA mis-splicing in disease. Nat. Rev. Genet. *17*, 19–32. https://doi.org/10.1038/nrg.2015.3.

Sehrawat, A., Gao, L., Wang, Y., Bankhead, A., McWeeney, S.K., King, C.J., Schwartzman, J., Urrutia, J., Bisson, W.H., Coleman, D.J., et al. (2018). LSD1 activates a lethal prostate cancer gene network independently of its demethylase function. Proc. Natl. Acad. Sci. USA *115*, E4179–E4188. https://doi.org/10.1073/pnas.1719168115.

Siedner, S., Krüger, M., Schroeter, M., Metzler, D., Roell, W., Fleischmann, B.K., Hescheler, J., Pfitzer, G., and Stehle, R. (2003). Developmental changes in contractility and sarcomeric proteins from the early embryonic to the adult stage in the mouse heart. J. Physiol. *548*, 493–505. https://doi.org/10.1113/jphysiol.2002.036509.

Speranzini, V., Rotili, D., Ciossani, G., Pilotto, S., Marrocco, B., Forgione, M., Lucidi, A., Forneris, F., Mehdipour, P., Velankar, S., et al. (2016). Polymyxins and quinazolines are LSD1/KDM1A inhibitors with unusual structural features. Sci. Adv. *2*, e1601017. https://doi.org/10.1126/sciadv.1601017.

Tamaoki, J., Takeuchi, M., Abe, R., Kaneko, H., Wada, T., Hino, S., Nakao, M., Furukawa, Y., and Kobayashi, M. (2020). Splicing- and demethylase-independent functions of LSD1 in zebrafish primitive hematopoiesis. Sci. Rep. *10*, 8521. https://doi.org/10.1038/s41598-020-65428-9.

Tian, T., Liu, Y., Yan, H., You, Q., Yi, X., Du, Z., Xu, W., and Su, Z. (2017). agriGO v2.0: a GO analysis toolkit for the agricultural community, 2017 update. Nucleic Acids Res. *45*, W122–W129. https://doi.org/10.1093/nar/gkx382.

Tochio, N., Umehara, T., Koshiba, S., Inoue, M., Yabuki, T., Aoki, M., Seki, E., Watanabe, S., Tomo, Y., Hanada, M., et al. (2006). Solution structure of the SWIRM domain of human histone demethylase LSD1. Structure *14*, 457–468. https://doi.org/10.1016/j.str.2005.12.004.

Toffolo, E., Rusconi, F., Paganini, L., Tortorici, M., Pilotto, S., Heise, C., Verpelli, C., Tedeschi, G., Maffioli, E., Sala, C., et al. (2014). Phosphorylation of neuronal Lysine-Specific Demethylase 1LSD1/KDM1A impairs transcriptional repression by regulating interaction with CoREST and histone deacetylases HDAC1/2. J. Neurochem. *128*, 603–616. https://doi.org/10.1111/jnc.12457.

Tosic, M., Allen, A., Willmann, D., Lepper, C., Kim, J., Duteil, D., and Schüle, R. (2018). Lsd1 regulates skeletal muscle regeneration and directs the fate of satellite cells. Nat. Comms. *9*, 366. https://doi.org/10.1038/s41467-017-02740-5.

Tunyasuvunakool, K., Adler, J., Wu, Z., Green, T., Zielinski, M., Žídek, A., Bridgland, A., Cowie, A., Meyer, C., Laydon, A., et al. (2021). Highly accurate protein structure prediction for the human proteome. Nature *596*, 590–596. https://doi.org/10.1038/s41586-021-03828-1.

Vara, C., Paytuví-Gallart, A., Cuartero, Y., Le Dily, F., Garcia, F., Salvà-Castro, J., Gómez-H, L., Julià, E., Moutinho, C., Aiese Cigliano, R., et al. (2019). Three-dimensional genomic structure and cohesin occupancy correlate with transcriptional activity during spermatogenesis. Cell Rep. *28*, 352–367.e9. https://doi.org/10.1016/j.celrep.2019.06.037.

Vinckier, N.K., Patel, N.A., Geusz, R.J., Wang, A., Wang, J., Matta, I., Harrington, A.R., Wortham, M., Wetton, N., Wang, J., et al. (2020). LSD1-mediated enhancer silencing attenuates retinoic acid signalling during pancreatic endocrine cell development. Nat. Comms. *11*, 2082. https://doi.org/10.1038/s41467-020-16017-x.

Vinyard, M.E., Su, C., Siegenfeld, A.P., Waterbury, A.L., Freedy, A.M., Gosavi, P.M., Park, Y., Kwan, E.E., Senzer, B.D., Doench, J.G., et al. (2019). CRISPR-suppressor scanning reveals a nonenzymatic role of LSD1 in AML. Nat. Chem. Biol. *15*, 529–539. https://doi.org/10.1038/s41589-019-0263-0.

Wang, J., Telese, F., Tan, Y., Li, W., Jin, C., He, X., Basnet, H., Ma, Q., Merkurjev, D., Zhu, X., et al. (2015). LSD1n is an H4K20 demethylase regulating memory formation via transcriptional elongation control. Nat. Neurosci. *18*, 1256–1264. https://doi.org/10.1038/nn.4069.

Wang, J., Hevi, S., Kurash, J.K., Lei, H., Gay, F., Bajko, J., Su, H., Sun, W., Chang, H., Xu, G., et al. (2008). The lysine demethylase LSD1 (KDM1) is required for maintenance of global DNA methylation. Nat. Genet. *41*, 125–129. https://doi.org/10.1038/ng.268.

Whyte, W.A., Bilodeau, S., Orlando, D.A., Hoke, H.A., Frampton, G.M., Foster, C.T., Cowley, S.M., and Young, R.A. (2013). Enhancer decommissioning by LSD1 during embryonic stem cell differentiation. Nature *482*, 221–225. https://doi.org/10.1038/nature10805.

Yu, G., Wang, L.-G., and He, Q.-Y. (2015). ChIPseeker: an R/Bioconductor package for ChIP peak annotation, comparison and visualization. Bioinformatics *31*, 2382–2383. https://doi.org/10.1093/bioinformatics/btv145.

Zhang, Y., Liu, T., Meyer, C.A., Eeckhoute, J., Johnson, D.S., Bernstein, B.E., Nusbaum, C., Myers, R.M., Brown, M., Li, W., and Liu, X.S. (2008). Model-based analysis of ChIP-seq (MACS). Genome Biol. *9*, R137. https://doi.org/10.1186/gb-2008-9-9-r137.

Zhu, D., Hölz, S., Metzger, E., Pavlovic, M., Jandausch, A., Jilg, C., Galgoczy, P., Herz, C., Moser, M., Metzger, D., et al. (2014). Lysine-specific demethylase 1 regulates differentiation onset and migration of trophoblast stem cells. Nat. Comms. *5*, 3174. https://doi.org/10.1038/ncomms4174.

Zibetti, C., Adamo, A., Binda, C., Forneris, F., Toffolo, E., Verpelli, C., Ginelli, E., Mattevi, A., Sala, C., and Battaglioli, E. (2010). Alternative splicing of the histone demethylase LSD1/KDM1 contributes to the modulation of neurite morphogenesis in the mammalian nervous system. J. Neurosci. *30*, 2521–2532. https://doi.org/10.1523/JNEUROSCI.5500-09.2010.

STAR★METHODS

KEY RESOURCES TABLE

REAGENT or RESOURCE	SOURCE	IDENTIFIER
Antibodies		
Mouse anti-OCT4	Thermo Fisher Scientific	Cat#MA1-104; RRID:AB_2536771
Rabbit anti-NANOG	Abcam	Cat#ab109250; RRID:AB_10863442
Rabbit anti-KDM1A	Abcam	Cat#ab17721; RRID:AB_443964
Rabbit anti-KDM1A	Abcam	Cat#ab129195; RRID:AB_11145494
Mouse anti-KDM1A	Abcam	Cat#ab31954; RRID:AB_776082
Mouse anti-FLAG	Sigma-Aldrich	Cat#A8592; RRID:AB_439702
Mouse anti-FLAG (FG4R)	Thermo Fisher Scientific	Cat#MA1-91878; RRID:AB_1957945
Rabbit anti-T7	Cell Signalling	Cat#13246; RRID:AB_2798161
Goat anti-T7	Abcam	Cat#ab9138; RRID:AB_307038
Mouse anti-Vinculin	Thermo Fisher Scientific	Cat#MS-1209-P0; RRID:AB_63659
Mouse anti-human Troponin2 (TNNT2)	Thermo Fisher Scientific	Cat#A25969
Rabbit anti-human NKX2.5	Thermo Fisher Scientific	Cat#A25974
Mouse anti-human Troponin2 (TNNT2)	Thermo Fisher Scientific	Cat#MS-295-P1; RRID:AB_61808
Rabbit anti-human NKX2.5	Cell Signalling	Cat#8792; RRID:AB_2797667
Rabbit anti-S-100	Abcam	Cat#ab868; RRID:AB_306716
Rabbit anti-Desmin	Abcam	Cat#ab15200; RRID:AB_301744
Mouse anti-Cytokeratin	Thermo Fisher Scientific	Cat#MA513203; RRID:AB_10942225
Goat-anti-rabbit IgG H&L (Alexa Fluor® 568)	Thermo Fisher Scientific	Cat#A11036; RRID:AB_10563566
Goat-anti-mouse IgG H&L (Alexa Fluor® 488)	Thermo Fisher Scientific	Cat#A11029; RRID:AB_2534088
Goat-anti-rabbit IgG H&L (Alexa Fluor®488)	Thermo Fisher Scientific	Cat#A11008; RRID:AB_143165
Goat-anti-mouse IgG H&L (Alexa Fluor® 568)	Thermo Fisher Scientific	Cat#A11004; RRID:AB_2534072
Goat-anti-mouse HRP	Promega	Cat#W4021; RRID:AB_430834
Goat-anti-rabbit HRP	Promega	Cat#W4011; RRID:AB_430833
Donkey-anti-goat HRP	Promega	Cat#W8051
Mouse anti-HDAC1	Cell Signalling	Cat#5356
Rabbit anti-HDAC1	Abcam	Cat#ab19845; RRID:AB_470299
Mouse anti-HDAC2	Cell Signalling	Cat#5113; RRID:AB_10624871
Rabbit anti-HDAC2	Abcam	Cat#32117; RRID:AB_732777
Rabbit anti-COREST	Millipore	Cat#07–455; RRID:AB_310629
Rabbit anti-RCOR2	Abcam	Cat#37113; RRID:AB_869950
Rabbit anti-RCOR3	Abcam	Cat#76921; RRID:AB_1523390
Rabbit anti-KDM1A (C69G12)	Cell Signalling	Cat#2184 RRID:AB_2070132
Bacterial and virus strains		
E. coli BL21(DE3) competent cells	Thermo Fisher Scientific	Cat#EC0114
Chemicals, peptides, and recombinant proteins		
Cas9 protein	PNABio	Cat#CP02
Lipofectamine 3000 Transfection Reagent	Thermo Fisher Scientific	Cat#L3000015
Puromycin Dihydrochloride	Thermo Fisher Scientific	Cat# A1113803
RN 1 dihydrochloride	R&D System	Cat# 4977/10
GSK-LSD1 inhibitor	Sigma-Aldrich	Cat# SML1072

(*Continued on next page*)

Continued

REAGENT or RESOURCE	SOURCE	IDENTIFIER
GeneScan 500 ROX dye Size Standard	Applied Biosystems	Cat#4310361
hESC-qualified Matrigel	Corning	Cat# CLS354277
16% Formaldehyde (w/v), Methanol-free	Thermo Fisher Scientific	Cat# 28906
O.C.T	VWR	Cat#361603E
Triton X-100	VWR	Cat#A16046-AE
Vitronectin (VTN-N) Recombinant Human Protein, Truncated	Thermo Fisher Scientific	Cat# A14700
Essential 8 Medium	Thermo Fisher Scientific	Cat#A1517001
RevitaCell Supplement	Thermo Fisher Scientific	Cat#A2644501
ProLong Gold antifade mounting solution with DAPI	Thermo Fisher Scientific	Cat#P36931
Gold	TED PELLA	Cressington 208HR
Protease inhibitor cocktail	Promega	Cat#G6521
Protein G Magnetic Beads	Thermo Fisher Scientific	Cat#88848
Anti-FLAG M2 affinity gel	Sigma-Aldrich	Cat#2220
3XFLAG- Peptide	Sigma-Aldrich	Cat# F3290
TaqMan™ Fast Advanced Master Mix	Thermo Fisher Scientific	Cat#4444557
Dynabeads Protein G	Thermo Fisher Scientific	Cat#10003
KaryoMAX™ Colcemid	Thermo Fisher Scientific	Cat# 15210040
Accutase	STEMCELL Technologies	Cat#07920
TRIzol	Thermo Fisher Scientific	Cat#15596026
21 amino acid H3 peptide	ChinaPeptide	N/A
peptide comprising the nine N-terminal residues of SNAI1	ChinaPeptide	N/A
GSK-090 non-covalent inhibitor	Laboratory of Antonello Mai	N/A
MC2652 tranylcypromine covalent inhibitor	Laboratory of Antonello Mai	N/A
GoTaq G2 Flexi DNA Polymerase	Promega	Cat#M7805
Critical commercial assays		
Precision gRNA Synthesis Kit	Thermo Fisher Scientific	Cat# A29377
Maxima H Minus cDNA Synthesis Master Mix with dsDNase kit	Thermo Fisher Scientific	Cat# M1682
Annexin V-FITC Apoptosis Staining and Detection Kit	Abcam	Cat# ab14085
Human Cardiomyocyte Immunocytochemistry Kit	Thermo Fisher Scientific	Cat# A25973
SuperScript VILO IV cDNA Synthesis Kit	Thermo Fisher Scientific	Cat#11754050
MicroPlex Library Preparation Kit v2	Diagenode	Cat#C05010012
Fluo-4 NW Calcium Assay Kit	Thermo Fisher Scientific	Cat# F36206
QIAquick PCR Purification Kit	Qiagen	Cat#28104
mRNA TruSeq Stranded library preparation KIT	Illumina	Cat#20020594
RNase-free DNase Set	Qiagen	Cat#79254
RNeasy Mini Kit	Qiagen	Cat#74106
Deposited data		
Raw and analyzed RNA-Seq and ChiP-Seq data	This paper	GEO: GSE189944
Raw RNA-Seq of human fetal heart	Pervolaraki et al. (2018)	Array Express archive from EMBL-EBI (ID: E-MTAB-7031)

(*Continued on next page*)

Continued

REAGENT or RESOURCE	SOURCE	IDENTIFIER
Mass SpectrometryTables. Related to Figure 6.	This paper, Mendeley Data	https://doi.org/10.17632/ts46ny74x7.1
Human reference genome NCBI build 38, GRCh38	Genome Reference Consortium	http://www.ncbi.nlm.nih.gov/projects/genome/assembly/grc/human/
Human Uniprot Database	EMBL-EBI	https://www.uniprot.org/proteomes/UP000005640
Atomic coordinates of the E2/Δ305COREST complex	This paper	Protein Data Bank (PDB), https://www.rcsb.org, Accession Code: PDB: 7ZRY
Original Western Blots	This paper	https://doi.org/10.17632/ts46ny74x7.1
Experimental models: Cell lines		
H1 WA01 Human embryonic stem cells (NIHhESC-10-0043)	WiCell	WAe001-A
Experimental models: Organisms/strains		
Mouse: C57BL/6N	The Jackson Laboratory	JAX: 000664
Mouse: NOD SCID gamma	Charles Rivers	614
Oligonucleotides		
gRNA targeting KDM1A exon 1: TCGG ACCAGCCGGCGCAAGC, see also Dataset S7	This paper	N/A
gRNA targeting KDM1A exon 2a: CTT CAAGACGACAGTTCTGG, see also Dataset S7	This paper	N/A
mKDM1A_Ex2_Fw: [6-FAM]AGTGAG CCGGAAGAGCCGTCTG	This paper	N/A
mKDM1A_Ex9_Rev: CTACCATTTCA TCTTTTTCTTTTGG	This paper	N/A
Primers for gRNA synthesis, see also Dataset S7	This paper	N/A
Taqman probes for qPCR assay, see Table S4	**This paper**	N/A
Recombinant DNA		
pTP6-FLAG-ubKDM1A	This paper	N/A
pTP6-FLAG-KDM1A+2a	This paper	N/A
pTP6-ubKDM1A-K661A	This paper	N/A
pTP6-KDM1A+2a-K661A	This paper	N/A
pTP6-3XT7-ubKDM1A	This paper	N/A
pTP6-3XT7-KDM1A+2a	This paper	N/A
His-SUMO-tagged Δ123KDM1A	Forneris et al., (2006)	N/A
GST-tagged Δ305CoREST1	Forneris et al., (2006)	N/A
pET15b-His$_8$-tagged ubKDM1A	This paper	N/A
pET15b-His$_8$-tagged KDM1A+2a	This paper	N/A
pTP6 Vector	Prattet al. (2000)	N/A
pET-15b Vector	Novagen (EMD Millipore)	Cat#69661–3
cDNA His$_8$-tagged ubKDM1A	Genewiz	N/A
cDNA His$_8$-tagged KDM1A+2a	Genewiz	N/A
cDNA 3XT7-ubKDM1A	Thermo Fisher Scientific	N/A
cDNA 3XT7-KDM1A+2a	Thermo Fisher Scientific	N/A

(*Continued on next page*)

Continued

REAGENT or RESOURCE	SOURCE	IDENTIFIER
Software and algorithms		
GeneMapper ID-X (version 1.6)	Thermo Fisher Scientific	https://www.thermofisher.com/order/catalog/product/A39975#/A39975
JuLI Stage software	NanoEntek	http://www.julistage.com
ImageJ	Open source	https://imagej.net
AlphaFold2	Open source	https://alphafold.ebi.ac.uk/
Mascot software	MatrixScience	https://www.matrixscience.com/
GraphPad Prism software	Graphstats	https://www.graphstats.net/graphpad-prism?gclid=CjwKCAiA78aNBhAlEiwA7B76pwONldupHqt08-AB7KNvUhS-Uwa2XAWsNg6nN41yEwMDl8TLsycj4BoCZGwQAvD_BwE
Artificial Intelligence RNA-Seq (AIR) Software	Sequentia Biotech	https://transcriptomics.cloud
R	The R Project	https://www.r-project.org/
FeatureCounts	Walter and Eliza Hall Institute of Medical Research	http://bioinf.wehi.edu.au/featureCounts
DESeq2	Bioconductor	https://bioconductor.org/packages/release/bioc/html/DESeq2.html
STAR	Alex Dobin, dobin@cshl.edu	https://groups.google.com/d/forum/rna-star
HTSFilter	Bioconductor	https://www.bioconductor.org/packages/release/bioc/html/HTSFilter.html
edgeR	Bioconductor	https://www.bioconductor.org/packages/release/bioc/html/edgeR.html
EnrichR	Open source	http://amp.pharm.mssm.edu/Enrichr/
BBDuk	BBTools Google Group: bbtools@lbl.gov	https://jgi.doe.gov/data-and-tools/bbtools/
FastQC	Babraham Bioinformatics Institute	https://www.bioinformatics.babraham.ac.uk/projects/fastqc/
Picard MarkDuplicates (version 2.8.1)	GitHub	http://broadinstitute.github
MACS2 (version 2.2.4)	Zhang et al. (2008)	https://pypi.org/project/MACS2/
bowtie2 (version 2.3.4.1)	Langmead et al. (2019)	https://sourceforge.net/projects/bowtie-bio/files/bowtie2/2.3.4.1/
Other		
Capillary electrophoresis Genetic Analyzer	Applied Biosystems	Model: 3130xl
LSRFortessa Cell Analyzer	BD Biosciences	N/A
EVOSTM XL Core microscope	Thermo Fisher Scientific	N/A
EVOSTM FL Auto 2 Imaging System	Thermo Fisher Scientific	N/A
JuLI™ Stage Real-Time Cell History Recorder	NanoEntek	N/A
LSM880, AxioObserver Z1, Laser scanning confocal microscope	Zeiss	N/A
EM CPD300 critical point drier	Leica	N/A
Scanning Electron Microscope Merlin	Zeiss	N/A
iBright^{TM} imaging system	Thermo Fisher Scientific	N/A
QuantStudio 3 Real-Time PCR System	Thermo Fisher Scientific	N/A
Q ExactiveTM Mass Spectrometer instrument	Sciex	N/A

RESOURCE AVAILABILITY

Lead contact

Further information and requests for sources and reagents should be directed to the lead contact, Antonio Adamo (Antonio.adamo@kaust.edu.sa).

Materials availability

All data are available in the manuscript text and supplemental information. hESC H1 line (WAe001-A) is available from WiCell. All the reagents and inhibitors used in this study are commercially available. This study did not generate new unique reagents. All newly plasmids and CRISPR-edited hESC lines generated in this study are available on request.

Data and code availability

- Both RNA-seq and ChiP-seq data generated for this work have been deposited in NCBI's Gene Expression Omnibus (GEO), and they are accessible through GEO accession number GSE189944. The sequencing depth, quality control (QC), and mapping reads are shown in Tables S5 and S6. The Atomic coordinates of the E2/Δ305COREST complex is available at Protein Data Bank (PDB), https://www.rcsb.org, with the following accession code: PDB: 7ZRY. Original western blot images have been deposited at Mendeley and are publicly available as of the date of publication. The DOI is listed in the key resources table. Microscopy data reported in this paper will be shared by the lead contact on request.
- The paper does not report original code.
- Any additional information required to reanalyze the data reported in this paper is available from the lead contact on request.

EXPERIMENTAL MODEL AND SUBJECT DETAILS

For heart developmental studies male and female C57BL/6N wild-type mice were used. Hearts were dissected at the indicated developmental stages. All experimental procedures entailing the use of rodents followed the guidelines established by the Italian Council on Animal Care (Legislative Decree no. 26, March 2014) and European regulations (2010/63/UE). For teratoma assays males and females NSG mice 8–10 weeksold were used. The use of mice for teratoma assay was approved by the Institutional Animal Care and Use Committee (IACUC number: IACUCRD #18-04-007). Every effort was made to minimize the number of mice used and their suffering. Human embryonic stem cell lines used in this study were incubated at 37 °C, 5% CO2. For crystallography studies proteins were expressed with an autoinducing protocol by using a *E. coli* BL21(DE3) strain cultured in LB medium at 37 °C.

METHOD DETAILS

hESC culture and cardiac differentiation

The hESC H1 (WA01) cell line used in this study was obtained from the WiCell bank. hESCs were cultured on vitronectin-coated (VTN, Thermo Fisher Scientific) and Essential 8 Medium (E8, Thermo Fisher Scientific), incubated at 37°C, 5% CO2 and passaged using Accutase (Thermo Fisher Scientific) and RevitaCell (Thermo Fisher Scientific). The PSC Cardiomyocyte Differentiation Kit (Thermo Fisher Scientific) was used for cardiomyocytes differentiation according to manufacturer's instruction. Fifteen, twelve and seven independent cardiomyocyte differentiation (up to 18–20 days) experiments have been performed in WT, KDM1A$^{-/-}$ and KDM1A+2a$^{-/-}$ cells, respectively. hESCs and derived cardiomyocytes were collected at different time points during differentiation and further processed for RNA or protein extraction. The differentiation of H1 into cardiac cells in presence of KDM1A inhibitors was performed by daily media change in presence of either 25 nM GSK-LSD1 (Sigma) or 25 nM RN-1 (R&D System) selective inhibitors. GSK-LSD1 is an inhibitor of KDM1A (IC50 = 16 nM) that is >1,000-fold selective over the closely related FAD-utilizing enzymes LSD2, MAO-A, and MAO-B. RN-1 is a cell-permeable tranylcypromine hydrochloride (TC) analog that has been reported to act as a potent inhibitor of KDM1A with a much lower IC50 (0.07 μM) than TC. RN-1 inhibits monoamine oxidase MAO-A and MAO-B with IC50 values of 0.51 and 2.79 μM, respectively (Cui et al., 2015; McGrath et al., 2016; Mohammad et al., 2015). Control H1 cells were differentiated in presence of DMSO alone (vehicle).

CRISPR-Cas9 mediated genome editing of the KDM1A gene

To achieve the full deletion of KDM1A and KDM1A+2a splicing variants a set of gRNAs were designed using http://crispr.mi.edu (Hsu et al., 2014), synthetized *in vitro* using the Precision gRNA Synthesis Kit (Thermo Fisher Scientific, A29377) according to the manufacturer's instructions and validated by T7 Indel assay using a T7 Endonuclease I (T7EI) digestion of the edited genomic region upon PCR amplification (González et al., 2014). The gRNAs with the highest T7 Indel score were transfected by Neon electroporation together with Cas9 protein (PNABio, 5 mg/mL, CP02) into H1 hESCs. Cells were harvested 72 h later and seeded at high dilution on vitronectin-coated plates. Individual clones were manually picked and transferred into 96-well for further Sanger sequencing validation and expansion. The gRNA targeting specificity was evaluated by PCR amplification and Sanger sequencing of the first two predicted off-target gRNA sites within gene exons. The DNA oligos used for gRNA synthesis, and PCR-mediated amplification of the targeted genomic regions are listed in Dataset S7.

Plasmids and constructs

pTP6-FLAG-ubKDM1A, pTP6-FLAG-KDM1A+2a and the enzymatically defective KDM1A-K661A plasmids were generated by using the EcoRI restriction site of the pTP6 vector (Pratt et al., 2000). The full-length KDM1A (amino acids 1–851) was inserted into the empty pTP6 vector to generate the pTP6-FLAG-ubKDM1A (Adamo et al., 2011). The full-length KDM1A+2a sequence (amino acids 1–871) was cloned into the empty pTP6 backbone to generate the pTP6-FLAG-KDM1A+2a. pTP6-3XT7-ubKDM1A and pTP6-3XT7-KDM1A+2a were obtained through EcoRI digestion and subcloning into the pTP6 vector of the 3XT7-ubKDM1A and 3XT7-KDM1A+2a sequences optimized for human expression (purchased from Thermo Fisher Scientific).

Codon optimized cDNAs encoding for N-terminally His_8-tagged ubKDM1A and KDM1A+2a were purchased from Genewiz and cloned inside a pET-15b vector. Plasmids for the expression of HisSUMO-tagged Δ123KDM1A and GST-tagged Δ305CoREST1 were produced as follows. HisSUMO-tagged Δ123KDM1A was cloned inside a pET-28a vector while GST-tagged Δ305CoREST1 was inserted in pGEX 6p1 plasmid (Forneris et al., 2006).

Plasmid stable transfection

To generate stable H1 KDM1A rescue clones, hESCs were transfected with either pTP6-FLAG-ubKDM1A, pTP6-FLAG-KDM1A+2a, pTP6-3XT7-ubKDM1A, pTP6-3XT7-KDM1A+2a, pTP6-ubKDM1A-K661A or pTP6-KDM1A+2a-K661A plasmids (2.5 ug) in presence of Lipofectamine 3000 (Thermo Fischer). Twenty-four hours after transfection hESCs have been selected with 1 mg/mL Puromycin (Thermo Fischer). Individual clones were manually picked and transfer to a 96-weel for further expansion.

Total RNA extraction from mice heart tissues

RNA extraction from murine samples was performed using TRIzol reagent (Thermo Fisher Scientific, 15596026) according to manufacturer's protocol. RNA was reverse transcribed using Maxima H Minus cDNA Synthesis Master Mix with dsDNase kit (Thermo Fisher Scientific, M1682). RT-PCR was conducted with GoTaq G2 Flexi DNA Polymerase (Promega, M7805) following standard PCR protocol.

Exon inclusion frequency by relative quantity fluorescent RT-PCR

Exon2a inclusion was quantified in mice hearts explanted at different developmental stages. RqfRT-PCR was used to measure E2a splicing inclusion in mature *Kdm1a* transcripts. All *Kdm1a* transcript isoforms were amplified in a single reaction using a fluorochrome-conjugated (FAM) forward primer annealing on Ex2 ([6-FAM]AGTGAGCCGGAAGAGCCGTCTG) and a reverse unmodified one annealing on Ex9 (CTACCATTTCATCTTTTTCTTTTGG). PCR products were mixed together with GeneScan 500 ROX dye Size Standard (Applied Biosystems, 4310361) and separated by capillary electrophoresis under denaturing conditions, using 3130xl Genetic Analyzer (Applied Biosystems). The relative amount of each amplified product was quantified as microsatellite sample, based on related fluorescence unit levels using the software using GeneMapper software (Zibetti et al., 2010).

Protein extraction from embryonic and postnatal mice hearts

Mouse embryonic and postnatal heart tissues were homogenized and total protein extracts were obtained lysing the tissues directly in Laemmli's sample buffer 1× supplemented with 2% 2-mercaptoethanol.

Immunoreactive bands were detected and quantified with UVITEC Alliance Mini HD9 (Cambridge). Antibodies used for Western blot are listed in the key resources table.

Teratoma assays

Wild-type H1 hESCs control and CRISPR-edited cell lines (passage 10–14) were injected subcutaneously into the dorsal flanks of NSG mice at 8–10 weeks of age. Approximately 1 × 10^6 cells were resuspended in 60μL of chilled Matrigel and PBS (v/v) and transplanted in each mouse. Teratomas of about 1 cm diameter were dissected (approximately 8–10 weeks after transplantation) and fixed in 4% formaldehyde. Samples were then O.C.T. embedded. Cross-sections were stained with hematoxylin and eosin or using antibodies specific for each germ layer (see key resource table). The use of mice for teratoma assay was approved by the Institutional Animal Care and Use Committee (IACUC number: IACUCRD #18-04-007).

Karyotype analysis

To induce mitotic arrest, cells were incubated in 5% CO_2 and 5% O_2 at 37°C in presence of 0.3 μg/mL KaryoMAX™ Colcemid™ for 15 min, then collected using Accutase for 4 min at 37°C. The cell pellet was resuspended in warm (37°C) 75mM Potassium Chloride solution and incubated at 37°C for 20 min before fixation with fixative solution (methanol:glacial acetic acid 3:1). The chromosomal G-band analysis was performed at the Cytogenetic Laboratory (Center of Excellence in Genomic Medicine Research, King Abdulaziz University, Jeddah SA). The analysis was performed counting at least 20 metaphases.

Annexin-V apoptotic assay and FACS analysis

To test the basal level of apoptosis or necrosis we used the Annexin V-FITC Apoptosis Staining and Detection Kit (Abcam, ab14085). Human ESCs seeded on vitronectin and grown in E8 for three days were detached according to the manufacturer's instructions and subjected to FACS analysis at LSRFortessa Cell Analyzer (BD Biosciences).

Immunofluorescence and microscopy acquisition

Undifferentiated hESCs were plated on vitronectin-coated coverslips and processed for immunofluorescence 72 h after seeding. Briefly, cells were fixed for 12 min with 3% paraformaldehyde at room temperature, permeabilized with 0.25% Triton X-100 in PBS, incubated overnight with primary antibodies in presence of blocking solution, washed, incubated with Alexa-Fluor conjugated secondary antibodies, and mounted with ProLong Gold antifade mounting solution (Thermo Fisher Scientific). hESC-derived cardiomyocytes were stained with the mouse Anti-Human TNNT2 and rabbit Anti-Human NKX2.5 antibodies using the Human Cardiomyocyte Immunocytochemistry Kit (Thermo Fisher Scientific, A25973) according to manufacturer's instructions.

Bright-field images were acquired using a phase contrast EVOS^{TM} XL Core microscope (Thermo Fisher Scientific) equipped with a 10× objective (Olympus). Immunostainings for pluripotency markers were acquired using an EVOS^{TM} FL Auto 2 Imaging System (Thermo Fisher Scientific) using a 1.30NA/40× oil immersion objective (Olympus). Immunostainings of hESC-derived cardiac cells were acquired using a laser scanning confocal microscope (LSM880, AxioObserver Z1, Zeiss) equipped with an Airyscan detector and a 1.4NA/60X oil objective (Zeiss), as Z-stacks of 0.3 μm steps, processed by maximum intensity projections and analyzed with ImageJ software.

Live imaging

Time-lapse images of control and KDM1A depleted hESCs were captured using an optical microscope (JuLI™ Stage Real-Time Cell History Recorder, NanoEntek) equipped with a high-sensitivity monochrome CCD (Sony sensor 2/3''), an automated x-y-z stage, and a 0.3 NA/10X objective (Olympus). hESCs were plated on vitronectin in presence of E8 Medium and recorded for 72 h at 60-min interval. The growth curve rate was automatically calculated on thresholded images, by measuring the total area occupied by the whole cells using the JuLI Stage software (NanoEntek).

For real-time imaging of beating cardiomyocytes, cells were recorded with the EVOS-FL Auto 2 Cell Imaging System (Thermo Fisher Scientific). During the acquisition cells were incubated at 37°C and 5% CO2 in a controlled stage incubator. Movies were acquired with an EVOS™10 × 0.30NA/7.13WD objective (Thermo Fisher Scientific).

Calcium live staining and kymograph analysis of beating cardiomyocytes

To evaluate the calcium waves of beating cells, hESCs were differentiated into cardiac cells on tissue culture plates. Beating cardiomyocytes (day 18–20 of differentiation) were incubated with 5 mM Fluo-4-AM (Thermo Fisher Scientific) for 30 min at 37°C before the acquisition. Cells were recorded in presence of differentiation media using the LED GFP light cube (Ex:470 nm, Em: 525 nm) of a fluorescent microscope equipped with a 37°C and 5% CO2 controlled stage incubator and a 10 × 0.30NA/7.13WD objective (EVOS-FL Auto 2 Cell Imaging System, Thermo Fisher Scientific). Time-lapses imaging were acquired for 30 seconds at 20 frames per second. The change in fluorescence intensity was analyzed by kymograph plots using ImageJ software. Kymographs were created by tracing a line of 300 μm along the distance axis on random fields of the movies. The waves of calcium spikes were measured from histograms of the mean fluorescence intensity over time obtained from each kymograph by using the command 'plot z-axis profile' of ImageJ. The amplitude of contraction was calculated as the average of the height from highest to lowest points of each mean fluorescence intensity peak divided by 2. The beat rate was measured as the ratio between the number of peaks from the mean fluorescence intensity histograms of individual areas and the time of acquisition (30 s).

Scanning electron microscopy (SEM) sample preparation and imaging

The cells were fixed with glutaraldehyde 1% in sodium cacodylate 0.1 M for 15 min, washed three times with sodium cacodylate 0.1 M for 5 min, and post-fixed with osmium tetroxide (OsO_4) 1% in sodium cacodylate 0.1 M for 20 min. After removing the OsO_4 solution and rinsing twice with bi-distilled water, the samples were gradually dehydrated through an ethanol series and dried using a Leica EM CPD300 critical point drier. Once dried, the samples were sputtered with a 10 nm layer of gold (TED PELLA, Cressington 208HR). The SEM images were acquired collecting the secondary electron (SE) signal, with a Zeiss Merlin (Oberkochen, Germany) microscope, equipped with a Schottky field emission gun working at an acceleration voltage of 5 kV and a beam current of 100 pA.

Co-immunoprecipitation assay

Immunoprecipitation from hESC total lysates was performed using approximately $10*10^6$ cells. hESCs were lysed using a low-stringency lysis buffer (50mM Tris-HCl, at pH 7.5, 120 mM NaCl, 0.5 mM EDTA, 0.5% Nonidet P-40 and 10% glycerol) in presence of a protease inhibitor cocktail (Promega, G6521) and about 1 mg of whole-cell extract was used for each immunoprecipitation (Adamo et al., 2011). Antibodies against T7, HDAC1, HDAC2, and control rabbit IgGs were used to carry out the immunoprecipitations overnight. Immunocomplexes were incubated with Protein G Magnetic Beads (Thermo Fisher Scientific, 88848) for 2 h, washed three times in washing buffer (50mM Tris-HCl at pH 8, 150 mM NaCl, 0.1% Triton, 5% glycerol and 0.5% dithiothreitol), eluted in loading buffer and separated by SDS-PAGE for immunoblotting.

Western blotting

Equal amounts of total cell extracts were separated by SDS–PAGE and transferred onto a nitrocellulose membrane (Amersham, GE Healthcare). Membranes were blocked with blocking solution (TBS containing 5% milk and 0.1% Tween), incubated with specific primary antibodies overnight at 4°C, washed four times in 5% milk in TBS-T, incubated with HRP-conjugated secondary antibodies and imaged on an iBright^{TM} imaging system (Thermo Fisher Scientific).

Mass spectrometry

Approximately 2 mg of total hESC total extract were immunoprecipitated in presence of Anti-FLAG M2 affinity gel (Sigma, 2220) overnight at 4°C and eluted with 3XFLAG- Peptide (Sigma, F3290) eluted in Elution Buffer (0.5M Tris-HCl, pH7.5, 1M NaCl) according to manufacturer's instructions. Immunoprecipitation eluates were denatured in loading buffer and separated by SDS-PAGE to about 1 cm. Proteins in gel bands were destained using 50 mM NH4HCO3 containing 50% ACN (v/v), dehydrated using 100% ACN and reduced by 10 mM dithiothreitol (DTT) in 100 mM NH4HCO3. Cysteine residues were alkylated using the IOA alkylating agent. Gel bands were subjected to a series of washing, dehydration, and hydration steps and then subjected to re-swelling overnight in gel Trypsin digestion steps. Trypsin digested proteins were isolated through supernatant collection by extraction buffers 5% acetic acid, 50% ACN and 0.1% TFA in 75% ACN. Samples were dried, reconstituted, and load on the Q ExactiveTM Mass Spectrometer instrument. The Mascot software was used to identify the peptide mass fingerprint from molecular ion peaks, sequence query and matched MS/MS ion spectra. The significant threshold was set at < 0.05, and the ion score of the expected cut-off was set at 20, the search was done through the Uniprot database, showing the percentage coverage, the number of significant matches and the number of peptide sequences.

RNA isolation, cDNA preparation, and reverse-transcription (RT)-PCR

For gene expression analyses, total RNA was extracted using the RNeasy Mini Kit according to manufacturer's instructions. DNase treatment was performed using RNase-free DNase Set. cDNA was synthesized with the SuperScript VILO IV cDNA Synthesis Kit. Gene expression was determined by real time qPCR on a QuantStudio 3 Real-Time PCR System using TaqMan™ Fast Advanced Master Mix and 10 μM TaqMan® Gene Expression Probes. Individual gene expression was normalized on TBP. The used TaqMan Gene Expression Probes are listed in Table S4.

Expression, purification, and crystallization

Full-length ubKDM1A and KDM1A+2a proteins were expressed with an autoinducing protocol by using a *E. coli* BL21(DE3) strain. GST-tagged Δ305CoREST1 containing plasmids was, instead, transformed in *E. coli* BL21(DE3) RPplus. Cells were grown in LB medium at 37 °C and 200 rpm till OD_{600}= 0.8. Protein expression was induced with O/N addition of 0.25 mM IPTG at 17 °C (Forneris et al., 2006). Cells were harvested at 5000 rpm 10°C for 10 min, flash frozen in liquid nitrogen and stored at -80 °C. Cells were disrupted by sonication and the suspension was clarified by centrifuging at 56000 × g, 4°C for 50 min. For purification, pellets of CoREST and KDM1A were resuspended together in 50 mM NaH_2PO_4 pH 8.0, 300 mM NaCl, 5% glycerol and 7.5 mM imidazole and subject to tandem affinity chromatography (HiTrap nickel column and GST-Trap) for co-purification of KDM1A/CoREST complexes (Forneris et al., 2006). The complexes were finally gel filtered through a Superdex 200 10/300 equilibrated in 25 mM KH_2PO_4 pH7.2, 5% glycerol. The concentration of KDM1A/CoREST was estimated by measuring the flavin absorbance at 458 nm (ϵ = 10790 $M^{-1}cm^{-1}$). Crystals were obtained through hanging drop vapor diffusion with a reservoir containing 1–1.3M Na/K tartrate and 0.1M ADA pH 6.5 (Forneris et al., 2006). The atomic coordinates of the complex between the full-length 2a splicing variant of human LSD1 and the N-terminally truncated Δ305 human CoREST were deposited with the Protein Data Bank (www.rcsb.org).

Activity toward peptides

Peptides were purchased from ChinaPeptides. Activity measurements were performed with peroxidase-coupled assays on a Clariostar plate reader (BMG Labtech). The reactions were carried out in 50 mM HEPES pH 8.5, 0.1 mM Amplex Red, 0.3 mM horseradish peroxidase, 0.3 μM KDM1A-CoREST. Peptidic substrates were serially diluted from 40 μM to 0.31 μM. Measured fluorescence signal reflects the enzymatic conversion of Amplex Red to resorufin. Non-linear regression analysis using GraphPad Prism software afforded the k_{cat} and K_M values.

Activity toward semisynthetic nucleosomes

To compare the activity of the different KDM1A complexes in the nucleosomal context, the method adopted by Pilotto et al., (2015) was used (Pilotto et al., 2015). Semisynthetics containing the Widom601 167 bp sequence and a recombinant H3 K4C-C110A double mutant were chemically modified to expose a propargylic group instead of the physiological dimethyl Lys4 side chain. The formation of the covalucleosomesome/KDM1A complex was visualized and quantified by size exclusion analytical chromatography performed on silica gel columns WTC-030N5 (Wyatt Technology, CA, USA) of 4.5 mL equilibrated in 15 mM TRIS/HCl pH 7.3, 0.4 mM EDTA, and 200 mM KCl at room temperature. KDM1A/CoREST (in 25 mM KH_2PO_4 pH 7.2, 5% glycerol) were mixed with semi-synthetic nucleosomes (in 20 mM Tris/HCl pH 7.5, 1 mM EDTA, 1 mM DTT) at 1:1.5 molar ratios and were incubated on ice for 2 h. Protein elution profiles were recorded with detection wavelengths set at 214 nm (peptide bond), 260 nm (DNA), and 280 nm (aromatic protein side chains) using an AKTAmicro purification system (GE Healthcare). To check the stability at the reaction conditions, each analyte is passed through the column alone.

Enzyme inhibition

Activity measurements were performed with peroxidase-coupled assays on a Clariostar plate reader (BMG Labtech). The reactions were carried out in 50 mM Hepes pH 8.5, 0.1 mM Amplex Red, 0.3 mM horseradish peroxidase, 0.3 μM KDM1A-CoREST, and 10 μM H3dimeK4 21 aa. 0.6 μM KDM1A/CoREST was first incubated for 10 min with serially diluted inhibitor in presence of 5% DMSO and in a total of 50 μL. After incubation, 50 μL of solution containing 20 μM substrate was added.

SNAI1 binding

The binding of SNAI1 to the KDM1A/CoREST complexes was estimated by fluorescence polarization (Speranzini et al., 2016). The assay mix contained 15 mM KH_2PO_4 pH 7.2, 5% glycerol, 0.01% Tween20, 10 nM SNAIL (1–9)-TAMRA. The peptide was titrated with increasing KDM1A/CoREST concentrations up 4 μM for a total of 16 points replicated three times each.

RNA-seq library preparation and sequencing

RNA libraries were generated using the human mRNA TruSeq Stranded library preparation KIT from Illumina, and profiled using HiSeq4000 and Novaseq 6000 SP1 systems (Illumina) with 150 bp paired-end sequencing method. An average of 50M reads was obtained for each sample. Samples with less than 15M input reads and lower than 81% assigned reads were removed from the analysis (Table S5).

RNA-seq data profiling

To analyze RNA-Seq data we used the Artificial Intelligence RNA-Seq (AIR) Software as a Service (SaaS) platform (https://transcriptomics.cloud) (Vara et al., 2019). RNA-Seq data validation, pairing and FastQC quality control was followed by trimming using BBDuk (Bushnell et al., 2017) and by setting a minimum read length of 35 bp and a minimum Phred-quality score of 25. After trimming quality control, high quality reads were mapped against the reference genome (GRCh38/Ensembl release 95) using the STAR end-to-end alignment method (Dobin et al., 2012) and gene expression quantification performed with featureCounts (Liao et al., 2014). The automated statistical analysis by AIR included a cleaning step for lowly expressed genes using HTSFilter (Rau et al., 2013). Genes with expression levels below the cut off (FPKM >1) were excluded from the analysis in agreement with EMBL-EBI guidelines (https://www.ebi.ac.uk/gxa/.html). For the identification of differentially expressed genes (DEGs) we used the statistical methods edgeR (Robinson et al., 2009). Data normalization was performed with the Trimmed Mean of M-values (TMM) method. Genes were considered differentially expressed if they had FDR<0.05 and LogFC ≥|0.5|. Six to four RNA-seq replicates per genotype were analyzed. Plots generated for data interpretation were the Principal Component analysis (PCA) for sample clustering, heatmaps showing the color-coded FPKM expression of selected groups of genes (Metsalu and Vilo, 2015), and Box Plot to compare single gene expression levels. GO enrichment analysis to identify the biological processes were performed with in-house scripts based on hypergeometric tests(Tian et al., 2017).

ChIP-sequencing libraries

ChIP for profiling KDM1A genome occupancy was performed using about 8×10^6 hESCs and 5×10^6 hESC-derived cardiac cells were used for each immunoprecipitation. Cells were detached using Accutase, fixed in PBS containing 1% formaldehyde and quenched with 125 mM glycine. Cells were lysed in ChIP lysis buffer (1% SDS, 10 mM EDTA and 50 mM Tris-HCl at pH 8.1) and sonicated (E220evolution Focused-ultrasonicator, Covaris) to generate 250-bp DNA fragments. Soluble chromatin was diluted eightfold in ChIP dilution buffer (0.01% SDS, 1.1% Triton X-100, 1.2 mM EDTA, 16.7 mM Tris-HCl at pH 8.1, and 167 mM NaCl). Chromatin was incubated overnight at 4°C with KDM1A or T7-tag antibodies and recovered using Dynabeads Protein G (Thermo Fisher Scientific). Beads were washed sequentially with buffers at different salt concentrations: low-salt wash buffer (0.1% SDS, 1% Triton X-100, 2 mM EDTA, 20 mM Tris-HCl (pH 8.1) and 150 mM NaCl), high-salt wash buffer (0.1% SDS, 1% Triton X-100, 2 mM EDTA, 20 mM Tris-HCl (pH 8.1) and 500 mM NaCl), lithium chloride wash buffer (0.25 M lithium chloride, 1% Nonidet P-40, 1% deoxycholate, 1 mM EDTA and 10 mM Tris-HCl (pH 8.1)) and TE buffer. Immunocomplexes were eluted in ChIP elution buffer (0.1% SDS, 1% Triton X-100, 2 mM EDTA, 20 mM Tris-HCl (pH 8.1) and 500 mM NaCl), at 30°C for 20 min and cross-linked overnight at 65°C (Adamo et al., 2014). DNA was purified using QIAquick PCR columns (Qiagen) according to the manufacturer's instructions. DNA libraries were generated using the MicroPlex Library Preparation Kit v2 (Diagenode) according to the manufacturer's instructions, and sequenced on the Illumina HiSeq 4000 or Novaseq 6000 SP1 platforms with 150 bp paired-end sequencing method.

ChIP-sequencing analysis

Raw data was quality-checked and trimmed with BBDuk (version December 10, 2015) (Bushnell et al., 2017) with a minimum read length of 35 bp and a minimum Phred quality score of 20. High-quality reads were then mapped against the human genome (GRCh38) using bowtie2 (version 2.3.4.1) (Langmead et al., 2019). Read duplicates were removed using Picard MarkDuplicates (version 2.8.1) [http://broadinstitute.

github]. Peak calling was performed using MACS2 (version 2.2.4) (Zhang et al., 2008) using default 'sharp' settings, setting the format of the tag file to "BAMPE." Peak annotation was carried out using the R package ChIPseeker (version 1.26.2) (Yu et al., 2015) with the UCSC knownGene annotation derived from the R package TxDb.Hsapiens.UCSC.hg38.knownGene. Peak annotation was further enriched for active or poised enhancers using H3K4m1 (ENCFF238YJA, ENCFF558IKG, ENCFF694ENI) and H3K27ac (ENCFF045CUG, ENCFF162HPV) ChIP-seq public data (https://www.encodeproject.org/). Thus, distal intergenic peaks overlapping with both H3K27ac and H3K4me1 peaks were annotated as active enhancers, whereas distal intergenic peaks overlapping only with H3K4m1 peaks were annotated as poised enhancers. ChIP-sequencing reads information before and after trimming and percentage of mapped reads are listed in Table S6.

Splicing variant analysis of human fetal cardiac samples

Paired-end read fastq files from 12 human fetal heart samples at three developmental stages: 9 weeks, 12 weeks, and 16 weeks obtained from a previously published dataset (Pervolaraki et al., 2018) available at the Array Express archive from EMBL-EBI (ID:E-MTAB-7031) or from H1 hESCs RNA generated in our lab (see Table S5) RNA-Seq data were quality controlled using FastQC (https://www.bioinformatics.babraham.ac.uk/projects/fastqc/); low quality reads and adaptors were trimmed using Cutadapt(Martin, 2011). Then, sequences were pseudo-aligned and quantified using Kallisto (Martin, 2011) (version 0.44.0 with default options) against the reference transcriptome from GrCh38 with sequence corresponding to *KDM1A* splicing transcripts: *ubKDM1A* (NM_015013.4), *nKDM1A+E8a* (NM_001363654.2), *nKDM1A+E2a+E8a* (NM_001009999), E2a transcript *KDM1A+E2a* (XM_005245786.2) was added to the index, to generate normalized transcript per million (TPM) values.

QUANTIFICATION AND STATISTICAL ANALYSIS

One-way ANOVA, Dunnett's post-hoc and post-hoc Tukey HSD analyses were used to test the significance between more than two groups. Alternatively, the non-parametric Student's t-*test* was used. Mean values ± STD or ±SEM are shown. *$p < 0.05$; **$p < 0.01$; ***$p < 0.001$. More statistical details of each experiment can be found in the figure legends.